PHYSICAL REVIEW B VOLUME 33, NUMBER 1 1 JANUARY 1986

Symmetry analysis and Monte Carlo study of a frustrated antiferromagnetic planar (XY) model in two dimensions

D. H. Lee,* J. D. Joannopoulos, and J. W. Negele
Department of Physics, Massachusetts Institute of Technology, Cambridge, Massachusetts 02139

D. P. Landau
Department of Physics, University of Georgia, Athens, Georgia 30602
(Received 30 April 1985)

The antiferromagnetic planar (XY) model on a triangular lattice is investigated using group-theoretical symmetry arguments combined with extensive Monte Carlo simulations and a detailed finite-size-scaling analysis. This approach allows for a systematic exploration of all possible symmetry-breaking transitions and their associated critical behavior. The entire magnetic-field—versus—temperature phase diagram is deduced. A rich class of possible new critical phenomena is obtained, including the introduction of a new multicritical point describing the confluence of the Ising and Kosterlitz-Thouless universality classes. The existence of the critical point is associated with a domain-wall-induced vortex-antivortex—unbinding transition.

I. INTRODUCTION

Frustrated two-dimensional spin systems exhibit exceedingly rich phase structure and critical phenomena, an example of which we study in this work by a combination of analytical analysis and numerical Monte Carlo calculations. One of the simplest of such frustrated systems is the antiferromagnetic planar (XY) model on a triangular lattice. From a theoretical perspective, this work is a natural step in the ongoing quest to understand the role of symmetry breaking and how rich structure arises from extremely simple fundamental interactions.

As a prelude to the new developments presented in this work, it is useful to briefly review the salient features of our prior understanding of the two-dimensional XY model. In 1966, the theorem of Mermin and Wagner[1] established that the continuous (global spin rotation) symmetry of the ferromagnetic planar, Heisenberg, and XY models in two dimensions (2D) could not be spontaneously broken at finite temperature. Here, there is no possibility of conventional long-range order at nonzero temperature, and any conventional order-disorder phase transition is thereby excluded.

Nevertheless, evidence accumulated suggesting some alternative form of phase transition. Results of high-temperature-series expansions[2-4] indicated that the fluctuations of the magnetization were diverging at a nonzero temperature. Moreover, low-temperature spin-wave calculations[5,6] yielded an algebraically decaying spin-spin correlation function and indicated the necessity of a phase transition from this behavior to the high-temperature regime where the correlations ought to decay exponentially.

The nature of this novel phase transition was explained by Kosterlitz and Thouless[7] with the introduction of the vortex and antivortex as the missing elementary excitations. At low temperature, the vortex and antivortex form bound pairs. These bound vortex pairs, together with the spin waves, destroy the spin long-range order, producing an algebraically decaying spin-spin correlation function. The transition occurs when the vortex pairs unbind. In the high-temperature phase, the spin-spin correlation decays exponentially with a correlation length defined by the mean distance between free vortices.

The Mermin-Wagner theorem, however, does not rule out the possibility of discrete symmetry breaking. This possibility was explored by Villain,[8] Stein and Cross,[9] Bak,[10] Alexander and Pincus,[11] and Nattermann[12] for a variety of systems described by Hamiltonians with continuous symmetry. Theoretical investigations of the nature of the phase transitions for such systems have not been carried out until very recently.[13-19] Teitel and Jayaprakash[13] studied the phase transitions of the 2D uniformly frustrated antiferromagnetic planar model by Monte Carlo simulation. This Hamiltonian, which models the Josephson coupling between superconducting islands in a square-lattice array in the presence of a transverse magnetic field, is given by

$$H = J \sum_{\langle ij \rangle} \cos(\theta_i - \theta_j - A_{ij}) , \tag{1}$$

where θ_i is the phase angle of the condensate wave function on the ith island. The constants A_{ij} introducing the frustration are physically determined by the line integral of the vector potential across the nearest-neighbor junction $\langle ij \rangle$,

$$A_{ij} = \frac{2e}{\hbar c} \int_i^j \mathbf{A} \cdot dl . \tag{2}$$

According to the results of Teitel and Jayaprakash,[13] for $\sum_P A_{ij} = \pi$ (where the sum is over all links in an elementary plaquette) there exists a temperature T_c at which the spin-wave—stiffness constant (which measures the stiffness of a system against a twisting of boundary spins) exhibits an apparent discontinuity larger than the Nelson-Kosterlitz[20] value $(2/\pi)T_c$. Moreover, the specific heat diverges at a temperature very close by. These two singularities were then identified with Kosterlitz-Thouless—type and Ising-type transitions, respectively. It was not clear from the simulations, however, whether or not these two transitions occur at different temperatures.

In a recent letter[15] the present authors used symmetry analyses and Monte Carlo simulations to describe the salient features of the phase diagram of the antiferromagnetic planar (AFP) model on a triangular lattice. In the case of zero field it was shown that, as a consequence of the breaking of a discrete symmetry, the system exhibits an additional discrete order parameter, the staggered helicity, and additional elementary excitations, the domain walls. A new spin disordering mechanism was proposed in which the interaction between the domain walls and the vortices causes the system to lose the quasi-long-range order (i.e., algebraically decaying correlation function) in the spin-spin correlation and long-range order in the staggered helicity correlation simultaneously at one transition temperature. At nonzero field, it was shown that the inherent frustration of the triangular lattice leads to a rich variety of phases and phase transitions. Independently, Miyashita and Shiba,[16] concentrating on the zero-field behavior of essentially the same model, have also pointed out the existence of discrete symmetry breaking and the existence of a discrete order parameter. Based on their simulation results, they find distinct Ising and Kosterlitz-Thouless transition temperatures that are within 2% of each other and argue that it is likely there is an intermediate phase between them.

In this paper we present a thorough discussion of the nature of critical phenomena of the AFP (XY) model on a triangular lattice using further symmetry analyses and additional Monte Carlo simulations. The format of the paper is as follows. In Sec. II we present a heuristic theory for the system in zero field. This simple theory establishes the framework within which the numerical results associated with the zero-field phase transition will be understood. In Sec. III we perform the symmetry analysis which enables us to understand the phase diagram and the phase transitions at nonzero field. In Sec. IV we present the Monte Carlo simulation results and analyze them in terms of the theories presented in Secs. II and III. Finally, Sec. V contains a summary and conclusions.

II. A HEURISTIC THEORY FOR ZERO FIELD

A. Ground state properties

The AFP model is specified by the following Hamiltonian:

$$\mathscr{H}=J\sum_{\langle \mathbf{RR}'\rangle}\mathbf{S}_{\mathbf{R}}\cdot\mathbf{S}_{\mathbf{R}'}=J\sum_{\langle ij\rangle}\cos(\theta_i-\theta_j)\ , \qquad (3)$$

where θ_i is the angle of a planar spin $\mathbf{S}_{\mathbf{R}_i}$ at site i, $\langle ij\rangle$ denotes nearest-neighbor pairs, and $J>0$. The ground states of (3) on a triangular lattice consist of spins ordered on three interpenetrating sublattices separated by lattice vectors of length $\sqrt{3}a$ (where a is the lattice constant) with spins on different sublattices oriented $\pm 120°$ with respect to each other. Typical ground-state $\sqrt{3}\times\sqrt{3}$ patterns are shown in Fig. 1.

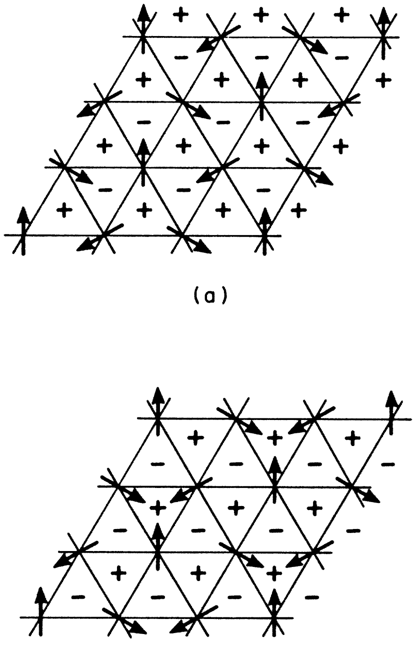

FIG. 1. Typical ground-state patterns for the triangular lattice at $H=0$. The plus or minus signs indicate the helicity of each triangle. The pattern shown in (b) cannot be obtained from (a) by a global spin rotation.

That these configurations are ground states can be easily proven using the following argument. Following Wannier,[17] consider the ground-state energy of any single elementary triangle of the lattice. By minimizing the energy with respect to two of the spin angles we obtain ground states for the triangle in which the spins form $\pm 120°$ angles with each other. It then follows that the $\sqrt{3}\times\sqrt{3}$ pattern is a ground state of the triangular lattice since each elemental triangle realizes its minimum-energy spin configuration. Finally, the $\pm 120°$ angle constraints force the ground state to have only $\sqrt{3}\times\sqrt{3}$ periodicity.

Unlike the ferromagnetic planar model, where the ground state only breaks global-spin-rotation symmetry, in the AFP model on a triangular lattice the ground state breaks an additional discrete symmetry. By comparing the ground-state patterns in Fig. 1, we note that there exist two topologically distinct classes of patterns characterized by different "helicity." To each triangle, we assign a helicity of $+1$, -1, or 0 defined as $\sum(\Delta\theta/2\pi)$, where $\Delta\theta$ is the smallest clockwise change in angle when the triangle is traversed in a clockwise direction.[21,22] Physically, the spins are rotated clockwise or counterclockwise for $+$ and $-$ helicity, respectively, as the triangle is traversed. Since global spin rotation conserves helicity, Fig. 1(b) cannot be obtained from Fig. 1(a) by pure rotation; it can only be obtained by including some other symmetry operation such as a lattice reflection. Although the spin patterns shown in Figs. 1(a) and 1(b) have similar orientational order, their helicity patterns are exactly out of phase. The staggered helicity η_s, defined as the staggered sum of the triangle helicities, therefore assumes the opposite sign for these two patterns. The staggered helicity and the $\sqrt{3}\times\sqrt{3}$ staggered magnetization serve as the two order parameters describing the system in zero field.

The existence of this extra discrete degeneracy is crucial, since it allows the system to support a third type of elementary excitation. In addition to spin waves and vortices, we have elementary excitations associated with domain-wall formation. Domain walls separating regions of opposite staggered helicity are shown in Fig. 2 where the interface is indicated by the dashed line. As a result of the opposite staggered helicity between the right and left domains, all the triangles cut by the interface have zero helicity.

Clearly, domain-wall excitations can destroy staggered helicity order. As we shall see later, vortices can alter the sign of the staggered helicity only locally so that they are much less effective in destroying staggered helicity order. Spin waves and vortices, on the other hand, are primarily responsible for destroying orientational spin order.

The thermodynamics of the AFP model on a triangular lattice will be determined by the interplay of these three types of elementary excitations. The ease of creating these excitations and their stability is of paramount importance in this regard. In Secs. II B and II C we shall consider the nature, energies and thermodynamic stability of domain-wall and vortex excitations. We will use this information in Sec. II D to estimate transition temperatures and develop a simple physical picture of the nature of the phase transitions in zero field.

B. Domain-wall excitations

Having recognized the existence of two topologically inequivalent ground states characterized by opposite staggered helicity, we now consider the nature of the boundaries between the states. The objective is to find the lowest-energy configurations corresponding to well-localized domain walls, determine the allowed orientations and stable shapes for the walls, evaluate the surface and corner energies, and thus obtain a description of the thermodynamics of low-lying helicity excitations.

Consider first the simplest case of a single straight boundary separating two domains of opposite staggered helicity. It is characterized by two distinct degrees of freedom: the orientation of the boundary on the lattice and the relative angle of rotation of the spins in these two domains. The minimum-energy configuration, with respect to boundary orientation and spin rotation, has been determined from a combination of analytical and numerical techniques. From this configuration, both the degree to which the spin disturbance is localized near the boundary and the surface energy have been determined.

A preliminary search for the optimal boundary orientation and relative spin rotation may be performed analytically by exploring a variety of natural boundary orientations, such as along lattice vectors or reciprocal-lattice vectors, and treating a single row of spins along the

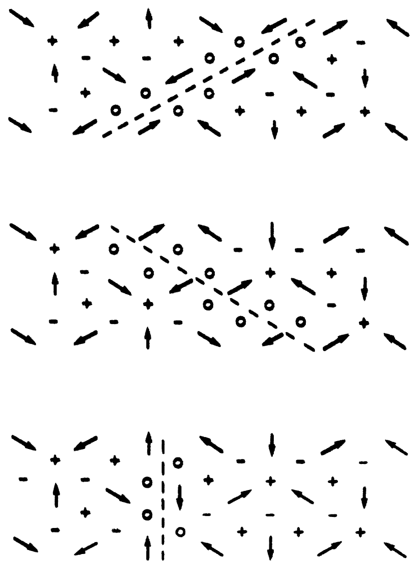

FIG. 2. Examples of domain walls separating regions of opposite staggered helicity. Triangles of spins with zero helicity form along the borders of the interfaces (dashed lines).

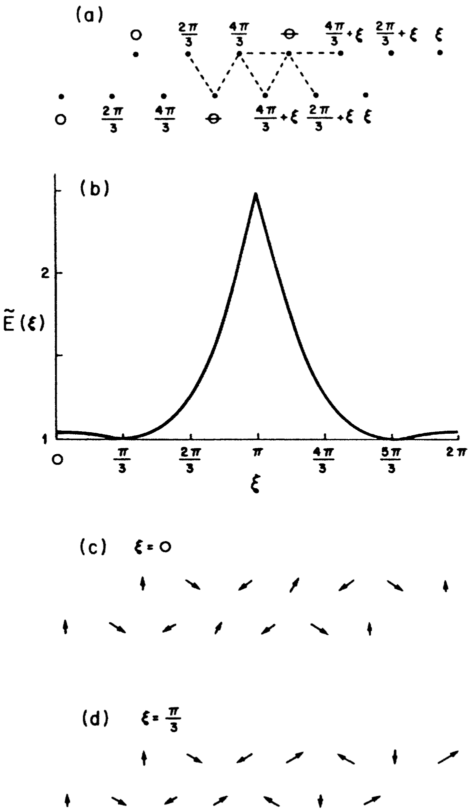

FIG. 3. Energies and spin configurations for a domain wall oriented parallel to a primitive reciprocal-lattice vector. (a) Angles of spins for a boundary oriented at 60° relative to the vertical axis. The angle ξ specifies the relative orientation of spins in the two staggered-helicity states. For fixed ξ the angle θ is allowed to minimize the energy: (b) Minimized domain-wall energy (for a segment of length $a\sqrt{3}$) in units of J as a function of angle ξ. (c) Spin configuration for $\xi=0$. (d) Spin configuration for minimum-energy geometry $\xi=\pi/3$.

boundary variationally. To determine, however, whether extended boundaries or alternative orientations yield lower energies, these studies have been complemented by numerical solutions on a large lattice. The spins at the upper and lower borders were set to positive and negative helicity states with a specified rotation angle, and periodic boundary conditions were applied on the left and right borders, displaced by an integral multiple of three lattice sites. The minimum-energy configuration was found by the method of simulated annealing:[23] spin configurations were generated according to the distribution $e^{-\beta H}$ using the Metropolis algorithm and β was gradually increased to isolate the ground state. Uniqueness was verified by repeated heating and cooling.

In this way the optimal boundary orientation was found to be parallel to the reciprocal lattice vectors. Figure 3(a) shows a boundary oriented at 60° relative to the vertical axis with the angle ξ specifying the relative orientation of spins in the two helicity states.

The surface energy associated with the boundary segment of level $\sqrt{3}a$ is given by the difference in energy of the seven nearest-neighbor bonds indicated by the dashed lines and seven bonds in the ground state. Minimization of E with respect to the variational parameter θ yields $\theta=\pi/3+\epsilon/2$, and the minimum energy, measured in units of the coupling constant J, is given by

$$\tilde{E}(\xi)=\pm 2\sqrt{3}\cos(\xi/2)+\cos\xi+\tfrac{7}{2}\ . \qquad (4)$$

This is plotted in Fig. 3(b).

The spin configuration for $\xi=0$, with $\tilde{E}=1.036$, is shown in Fig. 3(c). When all the spins are allowed to relax in a numerical solution with $\xi=0$, $\tilde{E}$ is lowered to 1.019 with the first, second, and third neighbors to site θ relaxing by 4.6°, 1.2°, and 0.4°, respectively.

As suggested by the graph in Fig. 3(b), the minimum energy occurs for $\xi=\pi/3$, with the configuration shown in Fig. 3(d). In contrast to the case of $\xi=0$, numerical calculations yield no relaxation. Hence, the optimal configuration has $\tilde{E}=1$ for a surface length of $\sqrt{3}a$ and spin precisely antialigned along the boundary.

1. Domain-wall configurations

The three equivalent minimum-energy orientations for domain walls are shown in Fig. 2. Note that by the $\sqrt{3}\times\sqrt{3}$ symmetry each boundary may be displaced by three lattice sites. The helicities for each plaquette are also shown, and using the definition in Sec. II A, the antialigned spins along the domain wall yield helicity zero for each plaquette touching the wall. Numerical calculations on a large lattice confirm that the angle and the domain-wall orientations in Fig. 2 are optimal. Whenever any other orientation is imposed by the boundary condition, the domain wall develops kinks as necessary in order to orient each segment along the directions shown in Fig. 2.

To complete the specification of domain-wall configurations, we now consider the possible stable kinks. In principle, according to Fig. 2, the lattice can support 60° and 120° intersections. An example of a 120° corner, composed of the upper two boundaries of Fig. 2, is shown in the top of Fig. 4 and has a corner energy (in excess of the surface energy) of $0.5J$. When a large lattice with boundary conditions to produce this corner is solved numerically, the spins relax to the configuration shown in the lower portion of Fig. 4, with a corner energy of $0.205J$. Note that the principal relaxation arises from the two spins nearest the corner rotating by approximately 19° to become nearly antiparallel. The distortion falls off rapidly with distance from the corner, with second- and third-nearest neighbors being rotated by the order of 9° and 4°, respectively. A similar calculation for a sharp 60° corner shows that it is unstable. Two walls intersecting in a single 60° corner will relax to a configuration with three straight walls and two stable 120° corners. The energy concentrated in the V-shape interface is too high, and it is energetically favorable to rotate the spins in the tip of the V and create an additional straight wall.

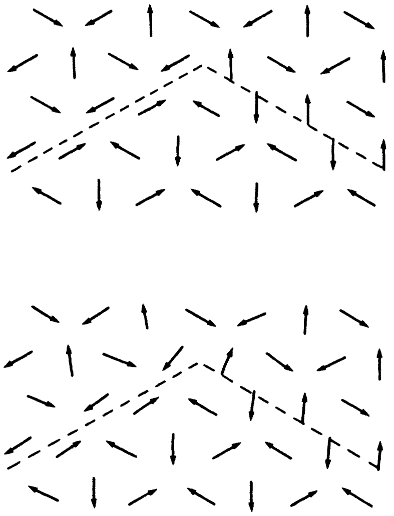

FIG. 4. Example of a domain wall with stable 120° corner in unrelaxed (top) and relaxed (bottom) configurations.

The optimal set of domain-wall configurations arising from this analysis is, thus, very simple and is summarized in Fig. 5. The set of optimal domain-wall orientations

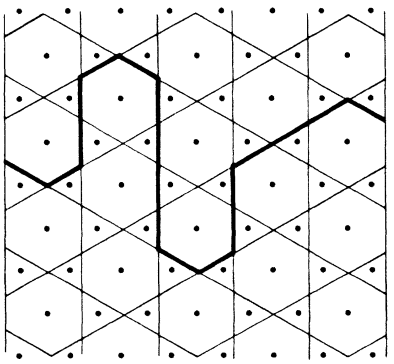

FIG. 5. Optimal domain-wall configurations on the triangular lattice. The walls can lie on a Kagome lattice as denoted by the thin solid lines but only 120° corners are stable. A typical configuration used to calculate the transition temperature is shown by the heavy solid line.

yields the Kagome lattice[24] denoted by the light solid lines. Stable walls correspond to all possible configurations having 120° kinks, and a typical example is shown by the heavy solid line. The surface energy of the wall is $J/\sqrt{3}a$ per unit length and the corner energy is $0.205J$.

2. Estimate of the transition temperature for domain walls

The estimate of the critical temperature T_w for domain walls on a Kagome lattice will be based on three simplifying approximations. The first approximation, following Müller-Hartmann and Zittarz,[25] is to ignore closed domain walls and consider only boundaries such as that shown in Fig. 5. The second approximation is to leave one end of the boundary constrained and calculate the entropy for all possible boundaries whose horizontal distance from the left edge is nondecreasing. We note that the validity of these approximations is not established in general. However, for Ising models we have checked that they yield the exact T_w for transitions on square and triangular lattices. The final approximation is to treat the corner energy perturbatively, which has also been verified to be accurate on a square lattice.

As a prelude to the more complicated case of a Kagome lattice, consider enumerating the unconstrained boundaries on a square lattice having nondecreasing horizontal distance. The most general boundary may be constructed by joining, head to tail with overlaps prohibited, horizontal vectors H pointing to the right, and vertical vectors V pointing up and down. We wish to count T_L, the number of branches of length L, obtained by connecting V's and H's in all possible ways. Let H_L and V_L denote the number of branches terminating in horizontal or vertical vectors, respectively. Then,

$$T_L = H_L + V_L \ . \tag{5}$$

Since each vertical vector (up or down) may connect to either a horizontal vector or vertical vector (up or down) and each horizontal vector may connect to upward vertical, downward vertical, and horizontal vectors, the possible connections are

$$\begin{aligned} V &\rightarrow VH \ , \\ H &\rightarrow VVH \ . \end{aligned} \tag{6}$$

Thus, since a V or H connects to a single H,

$$H_L = T_{L-1} \ , \tag{7}$$

and similarly

$$V_L = T_{L-1} + H_{L-1} \ . \tag{8}$$

Combining expressions (5), (7), and (8) yields the recursion relation

$$T_{L-2} = T_L - 2T_{L-1} \tag{9}$$

or

$$\begin{bmatrix} T_L \\ T_{L-1} \end{bmatrix} = \begin{bmatrix} 2 & 1 \\ 1 & 0 \end{bmatrix} \begin{bmatrix} T_{L-1} \\ T_{L-2} \end{bmatrix} \ . \tag{10}$$

The largest eigenvalue of the matrix in (10), $\lambda_+ = 1+\sqrt{2}$, dominates the number of branches for large L, so that

$$T_{L\rightarrow\infty} \simeq (\lambda_+)^L \ . \tag{11}$$

The critical temperature is given by the temperature at which the surface energy equals $k_B T$ times the entropy, so that using the surface energy $E_{\text{surf}} = 2J$ per unit length for the Ising model, we obtain

$$L E_{\text{surf}} = k_B T_w \ln(T_L) = k_B T_w L \ln\lambda_+ \ , \tag{12}$$

yielding the familiar result

$$k_B T_w = \frac{2J}{\ln(1+\sqrt{2})} \ . \tag{13}$$

The fundamental elements from which an unconstrained boundary may be built on a Kagome lattice with nondecreasing horizontal distance and 120° corners are shown in Fig. 6. In contrast to the square lattice with only two classes of vectors, H and V, the boundary is constructed from a sequence of oriented vectors classified A, B, C, and D. Note that, in determining allowed paths, one must distinguish the upper and lower and left and right sides of each hexagon of the Kagome lattice. The four generic connections for elements $A-D$ shown at the right generate all possible paths.

The number of distinct domain-wall boundaries is counted by enumerating all possible branches of length L constructed from the connections shown in Fig. 6. Let $A_L, \ldots, D_L$ denote the number of branches of length L terminating with elements $A, \ldots, D$, and let T_L denote the total number of branches of length L. Since each C can connect to two D's,

$$D_L = 2C_{L-1} \ . \tag{14}$$

Similarly, since both D and B connect to AC,

$$A_L = C_L = B_{L-1} + D_{L-1} \ , \tag{15}$$

and since A must connect to B,

$$B_L = A_{L-1} \ . \tag{16}$$

Combining these relations with the expression for the total number of branches,

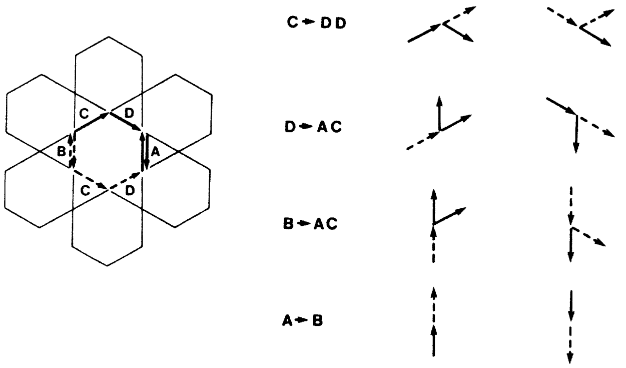

FIG. 6. The fundamental elements from which a domain wall may be built on a Kagome lattice with nondecreasing horizontal distance and 120° corners. The wall is constructed from a sequence of oriented vectors designated A, B, C, and D. The allowed choices of paths are shown.

$$T_L = A_L + B_L + C_L + D_L \ , \tag{17}$$

yields the recursion relation

$$T_{L+1} = 3T_{L-1} \ , \tag{18}$$

or

$$\begin{bmatrix} T_{L+1} \\ T_L \end{bmatrix} = \begin{bmatrix} 0 & 3 \\ 1 & 0 \end{bmatrix} \begin{bmatrix} T_L \\ T_{L-1} \end{bmatrix} . \tag{19}$$

In contrast to the case of the square lattice, both eigenvalues of the matrix in (19), $\lambda = \pm\sqrt{3}$, have the same magnitude. Note that the length of an element of the Kagome lattice is

$$L = \frac{a\sqrt{3}}{2} \ , \tag{20}$$

so that the surface energy per length L is

$$E_{\text{surf}} = L \frac{J}{a\sqrt{3}} = \tfrac{1}{2} J \ . \tag{21}$$

Hence, ignoring the corner energy, (12) yields the transition temperature for domain walls,

$$k_B T_w = \frac{E_{\text{surf}}}{\ln\lambda} = \frac{J}{\ln 3} \ . \tag{22}$$

Finally, we consider the effect of corner energy on T_w. For $E_{\text{corner}}/E_{\text{surf}} < 1$, we would expect to be able to estimate T_w perturbatively by simply replacing E_{surf} in (12) by $E_{\text{surf}} + P_{\text{corner}} E_{\text{corner}}$, where P_{corner} is the probability of a branch having a corner in a unit length in the limit of large L. For the case of a square lattice, we define P_L as the probability of having a corner in a unit length given a branch of length L. Then, by enumerating the corners added in each generation, it is straightforward to derive the recursion relation

$$P_{L+1} T_{L+1} (L+1) = 2P_L T_L L + P_{L-1} T_{L-1} (L-1) + 4T_{L-1} \ . \tag{23}$$

For large L, $P_L \rightarrow P_{\text{corner}}$. Solving for P_{corner} and using (9) gives

$$P_{\text{corner}} = \frac{4T_{L-1}}{T_{L-1} + T_{L-1}} \rightarrow 1 - \frac{1}{\lambda_+} \ . \tag{24}$$

Hence, the transition temperature, corrected to first order in E_{corner} for the square lattice, is given by

$$L\,(E_{\text{surf}} + P_{\text{corner}} E_{\text{corner}}) = k_B T_w L \ln\lambda_+ \tag{25}$$

or

$$k_B T_w = \frac{E_{\text{surf}} + E_{\text{corner}}[\sqrt{2}/(1+\sqrt{2})]}{\ln(1+\sqrt{2})} \ , \tag{26}$$

in agreement with an exact Müller-Hartmann Zittartz[25] calculation taken to first order in $E_{\text{surf}}/E_{\text{corner}}$.

For the Kagome lattice,[24] we can perform a similar calculation for P_{corner} using the generation pattern shown in Fig. 7. We note that the set (AC) always produces three sets of (AC) two generations later, consistent with the recursion relation (18). The number of corners generated in each connection is denoted by 0 or 1 in the figure. The corner probability $P_{L=2}$ is then obtained by observing that the six distinct branches of Fig. 7 result in a total of five corners for 12 segments of length L so that $P_2 = \frac{5}{12}$. Similarly, writing a recursion relation for further generations using Fig. 7 results in $P_{L>2}$ satisfying

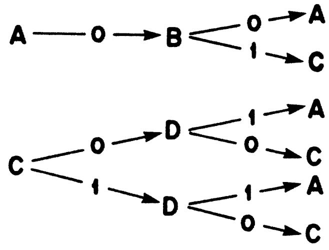

FIG. 7. The generation pattern used to calculate the corner probability as described in the text. The number of corners generated in each connection is denoted by 0 or 1.

$$P_{L+2}(L+2) = P_L L + \tfrac{7}{9} \ . \tag{27}$$

For large L we obtain simply

$$P_{\text{corner}} = \tfrac{7}{18} \ . \tag{28}$$

Hence, the final estimate for the transition temperature for domain walls, T_w, including the corner energy to first order, is

$$k_B T_w = \frac{E_{\text{surf}} + \frac{7}{18} E_{\text{corner}}}{\ln(\sqrt{3})} = \frac{\frac{1}{2}J + \frac{7}{18} \times 0.205J}{\ln\sqrt{3}} = 1.055J \ . \tag{29}$$

C. Vortex excitations and their stability

Vortices are elementary excitations associated with the orientation of the spins. Consequently, in this section we shall concentrate on the properties of the orientational order parameter only. In zero field, there are many possible definitions of the orientational order parameter which are physically equivalent, and we will subsequently discuss two particular choices. The essential requirements of any definition of the orientational order parameter ψ is that it be a maximum for the ground state, and when each spin is rotated by an angle δ then the angle θ between ψ and a reference axis is also increased by δ.

Since we are considering phenomena for which the length scale of the critical fluctuations becomes arbitrarily large relative to the lattice spacing, it is sufficient to consider the coarse-grained action $A(\psi)$. For an action invariant under global rotations, the low-lying excitations correspond to fluctuations in angle. Thus, we need consider the θ-dependent part of the action only. Moreover, global rotation symmetry restricts the action to be only a function of the derivatives of θ, and only derivatives consistent with spatial isotropy are to be included. Hence, the dominant term in the long-wavelength limit is given by

$$A = \int d^2 r \frac{\gamma}{2} [\nabla\theta(r)]^2 \ , \tag{30}$$

where the coefficient γ is called the spin-wave—stiffness constant or spin-helicity modulus.[26] The probability density for a particular $\{\theta\}$ is

$$e^{-A/k_BT}=\exp\left[-\left[\int d^2r\frac{\gamma}{2}[\nabla\theta(r)]^2/k_BT\right]\right] . \tag{31}$$

Let us assume that γ is known and proceed to determine the stability of a free vortex or antivortex. The vortex and antivortex are local minima of (30). A vortex (or antivortex) with its center located at (x_0,y_0) is described by the spin field

$$\theta_{\{ {v \atop a} \}}(\mathbf{r})=\pm\tan^{-1}\left[\frac{y-y_0}{x-x_0}\right] . \tag{32}$$

A spin orientation for a vortex-antivortex pair is illustrated in Fig. 8(a).

The cost in action to create a vortex is given by

$$\Delta A=\frac{\gamma}{2}\int d^2x(\nabla\theta_v)^2=\pi\gamma\ln\left[\frac{R}{a}\right] . \tag{33}$$

Here, R specifies the size of the system and a is a renormalization-group cutoff defining both the length scale above which fluctuations are considered and the value of the renormalized coupling constant γ. Since the center of the vortex core can be placed at any position, there is a large degeneracy factor associated with a single free-vortex configuration. For a two-dimensional system the degeneracy is roughly $(R/a)^2$. The total free energy for a single vortex is, therefore,

$$\Delta F=\pi\gamma\ln\left[\frac{R}{a}\right]-2k_BT\ln\left[\frac{R}{a}\right] . \tag{34}$$

Here $2k_B\ln(R/a)$ is the entropy associated with this configurational degeneracy. According to (34), when the temperature is raised above the critical temperature for vortices,

$$k_BT_v=\frac{\pi}{2}\gamma , \tag{35}$$

the system will spontaneously generate free vortices. At this temperature the system undergoes a phase transition.

In the above discussion we have neglected an important contribution to the free energy of a free vortex. This is the screening produced by bound vortex-antivortex pairs. Kosterlitz[7] took this into account by summing up the bound-pair contribution at all length scales. He showed that the contribution to the free energy from all bound pairs with vortex-antivortex separation less than a given length amounted to a renormalization of the spin-wave—stiffness constant and the chemical potential of the vortex core. In the renormalized theory, the transition thus occurs at

$$k_BT_v=\left[\frac{\pi}{2}\right]\gamma_R , \tag{36}$$

where γ_R is the renormalized spin-wave—stiffness constant obtained in the limit as the lower cutoff $a\rightarrow\infty$.

At a fixed temperature, the spin-wave—stiffness constant γ of a system on a discrete lattice can be determined by the following procedure. Let us consider a system composed of $N\times N$ planar spins (N spins in each basis vector direction). Let us impose the following two types of boundary condition: boundary condition (a),

$$\theta(\mathbf{r}+N\hat{\mathbf{e}}_1)=\theta(\mathbf{r}),\quad \theta(\mathbf{r}+N\hat{\mathbf{e}}_2)=\theta(\mathbf{r}) \tag{37}$$

and boundary condition (b),

$$\theta(\mathbf{r}+N\hat{\mathbf{e}}_1)=\theta(\mathbf{r})-N\Delta,\quad \theta(\mathbf{r}+N\hat{\mathbf{e}}_2)=\theta(\mathbf{r}) . \tag{38}$$

Here $\hat{\mathbf{e}}_1$ and $\hat{\mathbf{e}}_2$ are the two basis vectors. The spin-wave—stiffness constant is then given by

$$\gamma=\lim_{\Delta\rightarrow\sigma}\left[\frac{2\rho}{\Delta^2N^2}(F_b-F_a)\right] , \tag{39}$$

where F_a,F_b are the free energies of the system under boundary conditions (a) and (b), respectively, and ρ is the areal density of the spins. It is shown in Appendix A that for the triangular lattice (39) leads to

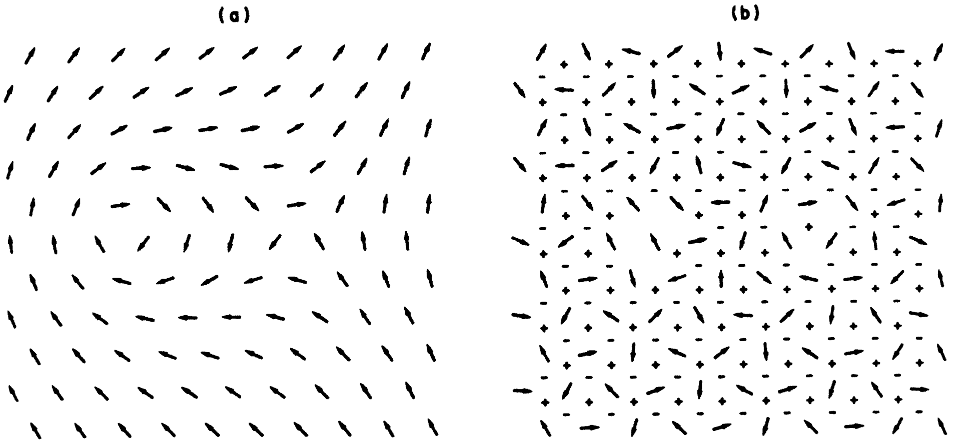

FIG. 8. Illustration of a simple vortex-antivortex excitation built on a $\sqrt{3}\times\sqrt{3}$ ground state in the (a) $\{\psi(\mathbf{R})\}$ and (b) $\{\mathbf{S}(\mathbf{R})\}$ representations as described in the text.

$$\gamma = -\frac{1}{\sqrt{3}}\langle u \rangle - \frac{2J^2}{\sqrt{3}TN^2k_B}\left[\sum_{\langle ij \rangle}\sin(\theta_i-\theta_j)\hat{e}_{ij}\cdot\hat{e}_1\right]^2 . \tag{40}$$

Here $\langle\ \rangle$ denotes a thermal average under the periodic condition (a), $\langle u \rangle$ is the averaged energy per spin, J is the spin constant in the Hamiltonian, and $\hat{e}_{ij}$ is the unit vector pointing from site j to site i. At zero temperature (40) gives a spin-wave—stiffness constant

$$\gamma = \frac{\sqrt{3}}{2}J . \tag{41}$$

Therefore, the unrenormalized theory will predict a Kosterlitz-Thouless transition at

$$k_BT_v = \frac{\pi}{2}\frac{\sqrt{3}}{2} = 1.36J . \tag{42}$$

Finally, we conclude by presenting two specific definitions of the orientational order parameter $\psi(\mathbf{R})$ on a triangular lattice. The first definition is

$$\psi_{\pm}(\mathbf{R}) = \begin{cases} \mathbf{S}_{\mathbf{R}}, & \{\mathbf{R}\} \text{ in sublattice 1} \\ \mathcal{R}^{\pm}\mathbf{S}_{\mathbf{R}} & \{\mathbf{R}\} \text{ in sublattice 2} \\ \mathcal{R}^{\mp}\mathbf{S}_{\mathbf{R}} & \{\mathbf{R}\} \text{ in sublattice 3} \end{cases} \tag{43}$$

where $\mathcal{R}^{+}$ denotes a rotation of $\pm(2\pi/3)$ and 1, 3, and 3 refer to the three sublattices defining the $\sqrt{3}\times\sqrt{3}$ symmetry. The definitions of $\psi_{+}(\mathbf{R})$ and $\psi_{-}(\mathbf{r})$ map the antiferromagnetic ground states (of opposite staggered helicity) onto the ferromagnetic ground state. The advantage of these definitions is that they reveal the topological structure of excitations which are built on one of these ground states. As an illustration, in Fig. 8 we show how a simple vortex-antivortex excitation built on a $\sqrt{3}\times\sqrt{3}$ ground state appears in the $\{\mathbf{S}(\mathbf{R})\}$ and $\{\psi(\mathbf{R})\}$ representations. Unfortunately, this order parameter is not particularly illuminating in the presence of domains of opposite staggered helicity, since excitations in only half of the domains are intelligibly "decoded."

The second orientational order parameter is defined on the sites $\mathbf{R}$ of a $\sqrt{3}\times\sqrt{3}$ sublattice as follows:

$$\psi(\mathbf{R}) = \mathbf{S}(\mathbf{R}) - \tfrac{1}{2}\mathbf{S}(\mathbf{R}+\hat{e}_1) - \tfrac{1}{2}\mathbf{S}(\mathbf{R}+\hat{e}_2) . \tag{44}$$

This definition arises naturally as one component of the order parameter obtained by the subsequent symmetry analysis in Sec. III B, and will be used to study the critical behavior associated with orientational order in numerical calculations.

D. Physical estimates of transitions

The most straightforward interpretation of the results obtained in Secs. II B and II C suggests that there exist two transitions. One, at a lower temperature $k_BT_w \sim 1.1J$, is associated with the destruction of the staggered helicity long-range order, and the other, at a higher temperature $k_BT_v \sim 1.4J$, is associated with the destruction of the spin quasi-long-range order. However, in these calculations we have neglected fluctuations like spin waves, higher-energy domain walls, bound vortex pairs, and most importantly the interaction between the domain walls and vortices. The contribution of higher-energy domain walls and spin waves to the surface free energy will shift the value of T_w to T'_w and the contribution of spin waves and bound vortex pairs to the vortex free energy will shift T_v and T'_v. However, given the separation of T_w and T_v and the physical foundation of our estimate, we believe that T'_w could be below T'_v.

In addition to these quantitative shifts in T_w and T_v, the interaction between domain walls and vortices can produce a qualitative change in the physics above T_w. The domain wall can act like a grain boundary and release the strain produced by the dislocations (vortices). Above T_w, the proliferation of domain walls could thus induce pair unbinding and thereby drive the Kosterlitz-Thouless transition. This, in fact, is what we believe is happening in the AFP model on the triangular lattice. (Halsey[19] has recently reached a similar conclusion in studying the phase transition for the fully frustrated antiferromagnetic planar model on a square lattice.) It should be noted that a domain-wall—induced pair-unbinding mechanism is fundamentally different from the pure pair unbinding in the Kosterlitz-Thouless theory.

III. THEORETICAL ANALYSIS FOR NONZERO FIELD

A. Ground-state properties

The Hamiltonian in the presence of an in-plane magnetic field $\mathbf{H}$ is given by

$$\mathcal{H} = \sum_{\langle \mathbf{RR}' \rangle} J_{\mathbf{RR}'}\mathbf{S}_{\mathbf{R}}\cdot\mathbf{S}_{\mathbf{R}'} - \sum_{\mathbf{R}}\mathbf{H}\cdot\mathbf{S}_{\mathbf{R}} . \tag{45}$$

As in the case of zero field, it is shown in Appendix B that the ground states preserve the three-sublattice structure with $\sqrt{3}\times\sqrt{3}$ periodicity and that the sublattice magnetizations $\mathbf{m}_1,\mathbf{m}_2,\mathbf{m}_3$ satisfy the following equation:

$$\mathbf{m}_1+\mathbf{m}_2+\mathbf{m}_3 = \mathbf{H}/3J . \tag{46}$$

Geometrically, this means that the sublattice magnetizations $\mathbf{m}_1,\mathbf{m}_2,\mathbf{m}_3$ must lie on two unit circles separated by $H/3J$.[14] Two typical solutions are illustrated in Fig. 9(a) for a field $H<3J$. The middle vector is accentuated in the diagram since its position uniquely determines the direction of the other two vectors. Note that a reflection about the direction of the external field changes the sign of the helicity of the triad. A set of continuously connected solutions is defined by the configurations accessible by sliding the middle vector with its end constrained on the two circles. Such a set is illustrated by the orientations labeled 1–6 in the first diagram in Fig. 9(b).

There are two critical fields associated with (45). The first is given by $H=3J$. For $H<3J$ any triad configuration has a specific helicity state that is maintained as the vectors slide around. Above $H=3J$, however, starting with any triad configuration one can generate its mirror image through continuous sliding. The value $H=3J$ therefore represents the transition at which the additional discrete degeneracy associated with the helicity ordering disappears. The other singular point is given by $H=9J$.

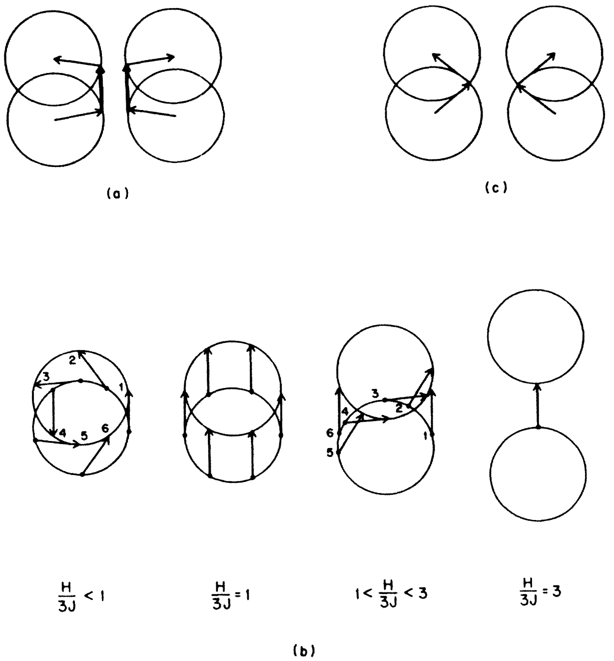

FIG. 9. (a) Typical ground-state pattern for the AFP model on a triangular lattice in the presence of a uniform magnetic field (pointing up). The three sublattice magnetizations are constrained such that the ends of the middle vector are confined to the two circles. The middle vector is accentuated since its position uniquely determines the direction of the other two vectors. An infinite degeneracy for the ground state is possible. (b) Sets of degenerate solutions (labeled 1–6) obtained by sliding the middle vector for various values of the magnetic field. Two critical fields at $H=3J$ and $H=9J$ can be identified. (c) Typical ground-state patterns for the AFP model on a square lattice in the presence of a field. The arrows represent the two sublattice magnetizations and are constrained to lie at the intersections of the two circles as shown. Only twofold degeneracy is possible.

At this value of the field, the distance between the center of the circles is 3 times the radius. The only solution is $\mathbf{m}_1=\mathbf{m}_2=\mathbf{m}_3=\mathbf{H}/9J$, and $H=9J$ thus represents a transition at which the system becomes paramagnetic.

Unlike the case of the AFP model on a square lattice [Fig. 9(c)], where the external field immediately removes the continuous degeneracy, the triangular-lattice ground states remain continuously degenerate even in the presence of an external field. However, it is important to note that this degeneracy is not dictated by a symmetry on the Hamiltonian, so that there are no associated Goldstone modes[27] which destroy spin long-range order. Because there is no symmetry in the Hamiltonian, this degeneracy will not appear in the free energy even at the lowest temperature.

B. Order parameter

We have seen that the ground state of the AFP model maintains a $\sqrt{3}\times\sqrt{3}$ periodicity [Fig. 10(a)] in the presence of a uniform magnetic field. In reciprocal space, the k points consistent with this periodicity are $\pm\mathbf{q}_0=(\pm4\pi/3a,0)$ located at the Brillouin-zone corners as shown in Fig. 10(b). Thus, a natural choice for an order parameter that will measure this periodicity is given by

$$\boldsymbol{\psi}_{\mathbf{q}_0}=\frac{1}{N}\sum_{\mathbf{R}}e^{-i\mathbf{q}_0\cdot\mathbf{R}}\mathbf{S}_{\mathbf{R}}\,. \tag{47}$$

An additional motivation for this choice is the behavior of the Fourier transform of the coupling matrix $J_{\mathbf{RR}'}$, shown in Fig. 10(c), which attains its minimum value at $\pm\mathbf{q}_0$. If one expresses the partition function for the antiferromagnet as a functional integral over an auxiliary field using the Hubbard-Stratonovich transformation, it is straightforward to see that the first component of the quadratic form to become critical as the temperature is increased is the Fourier component corresponding to the most negative value of the coupling matrix. Note also, from a purely symmetry point of view, $\mathbf{q}_0$ and $-\mathbf{q}_0$ form a star which satisfies the Lifshitz condition[28] and are therefore consistent with the assumed commensurate transition.

The order parameter $\boldsymbol{\psi}$ constructed in this way is a two-component complex vector with $\boldsymbol{\psi}_{\mathbf{q}_0}=\boldsymbol{\psi}^*_{-\mathbf{q}_0}$ since the spin field is real. For convenience, let us further define

$$\boldsymbol{\psi}_{\mathbf{q}_0}=\begin{bmatrix}\sigma_{\parallel}+i\tau_{\parallel}\\ \sigma_{\perp}+i\tau_{\perp}\end{bmatrix}\equiv\begin{bmatrix}\sigma_{\parallel}\\ \tau_{\parallel}\\ \sigma_{\perp}\\ \tau_{\perp}\end{bmatrix}, \tag{48}$$

where the parallel and perpendicular components are tak-

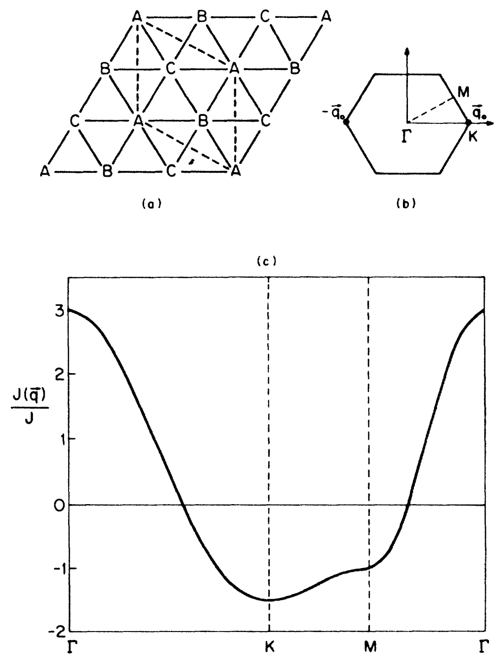

FIG. 10. (a) Illustrations of the three sublattices (labeled A, B, and C) and the unit cell of the triangular lattice having $\sqrt{3}\times\sqrt{3}$ periodicity. (b) Brillouin zone for the triangular lattice. The points $\pm\mathbf{q}_0$ represent primitive reciprocal-lattice vectors with $\sqrt{3}\times\sqrt{3}$ periodicity. (c) Fourier transform of coupling constant $J_{\mathbf{RR}'}$ along symmetry directions of the Brillouin zone.

en with respect to the direction of the external field.

If we denote by $\mathbf{S}^{(1)}$ the average of the spins on the sublattice containing the origin of $\mathbf{R}$ in the sum in (47) and by $\mathbf{S}^{(2)}$ and $\mathbf{S}^{(3)}$ the average of the spins on the other two sublattices, then from (47) and (48) it follows that

$$\begin{aligned}\sigma_{\{\substack{\parallel\\ \perp}\}}&=S^{(1)}_{\{\substack{\parallel\\ \perp}\}}-\tfrac{1}{2}S^{(2)}_{\{\substack{\parallel\\ \perp}\}}-\tfrac{1}{2}S^{(3)}_{\{\substack{\parallel\\ \perp}\}}\ ,\\ \tau_{\{\substack{\parallel\\ \perp}\}}&=\frac{\sqrt{3}}{2}S^{(2)}_{\{\substack{\parallel\\ \perp}\}}-\frac{\sqrt{3}}{2}S^{(3)}_{\{\substack{\parallel\\ \perp}\}}\ .\end{aligned}\qquad(49)$$

These relative weightings of the sublattices in σ and τ are depicted schematically in Fig. 11. Note, for future reference, that defining the origin in the sum over R on any sublattice is physically equivalent, so that an equivalent order parameter is obtained by cyclic permutations of the sublattices in (49) or, equivalently, by multiplying the column vector $\binom{\sigma}{\tau}$ by a rotation matrix for ±120°.

The helicity order parameter defined earlier[22] can be expressed in momentum space as follows:

$$\begin{aligned}\eta_s=\sum_{\mathbf{R}}\sum_{\mathbf{q}}\sum_{\mathbf{q}}&(\boldsymbol{\psi}_{\mathbf{q}}e^{i\mathbf{q}\cdot\mathbf{R}}\boldsymbol{\psi}_{\mathbf{q}'}e^{i\mathbf{q}'\cdot(\mathbf{R}+\hat{\mathbf{e}}_1)}\\ &+\boldsymbol{\psi}_{\mathbf{q}}e^{i\mathbf{q}\cdot(\mathbf{R}+\hat{\mathbf{e}}_1)}\boldsymbol{\psi}_{\mathbf{q}'}e^{i\mathbf{q}'\cdot(\mathbf{R}+\hat{\mathbf{e}}_2)}\\ &+\boldsymbol{\psi}_{\mathbf{q}}e^{i\mathbf{q}\cdot(\mathbf{R}+\hat{\mathbf{e}}_2)}\boldsymbol{\psi}_{\mathbf{q}'}e^{i\mathbf{q}'\cdot\mathbf{R}})\cdot\hat{\mathbf{z}}\\ =\sum_{\mathbf{q}}&S(\mathbf{q})\,\mathrm{Im}(\psi^{\parallel}_{\mathbf{q}}\psi^{\perp *}_{\mathbf{q}})\ ,\end{aligned}\qquad(50)$$

where

$$\begin{aligned}S(\mathbf{q})=2\sin&\left[\left[\tfrac{1}{2}q_x+\frac{\sqrt{3}}{2}q_y\right]a\right]\\ &+\sin\left[\left[\tfrac{1}{2}q_x-\frac{\sqrt{3}}{2}q_y\right]a\right]-\sin(q_xa)\ .\end{aligned}\qquad(51)$$

When the spin configuration manifests $\sqrt{3}\times\sqrt{3}$ symmetry; it follows that $\mathrm{Im}(\psi^{\parallel}_{\mathbf{q}_0}\psi^{\perp}_{\mathbf{q}_0})$ measures the helicity.

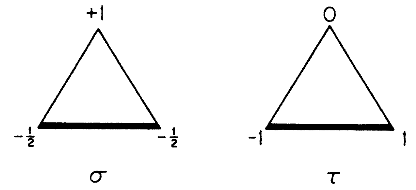

FIG. 11. The projection of σ and τ on three sublattices as discussed in the text.

C. Symmetry analysis

In the presence of the field, the symmetry group of the Hamiltonian (45) is

$$G=T\times C_{6v}\times C_s^{(\mathrm{spin})}\ ,\qquad(52)$$

where T is the translation group of the triangular lattice [Fig. 12(a)],

$$T\equiv\{m\hat{\mathbf{e}}_1+n\hat{\mathbf{e}}_2;\ m,n=\text{integer}\}\ .\qquad(53)$$

C_{6v} is the point group of the triangular lattice [Fig. 12(b)],

$$C_{6v}=\{E,2C_6,2C_3,C_2,3\sigma_v,3\sigma_d\}\ ,\qquad(54)$$

and $C_s^{(\mathrm{spin})}$ is a group associated with the spins containing the identity and a reflection of a spin about the direction of the magnetic field [Fig. 12(c)],

$$C_s^{(\mathrm{spin})}=\{E,\sigma\}\ .\qquad(55)$$

The order parameter defined in (47) forms a basis for representation of the Hamiltonian symmetry group. Under translation, the translated order parameter is the Fourier transform of the translated spin pattern. Therefore,

$$\boldsymbol{\psi}'_{\mathbf{q}_0}=T_{\mathbf{a}}\boldsymbol{\psi}_{\mathbf{q}_0}=\sum_{\mathbf{R}}e^{-i\mathbf{q}_0\cdot\mathbf{R}}\mathbf{S}_{\mathbf{R}-\mathbf{a}}=e^{-i\mathbf{q}_0\cdot\mathbf{a}}\boldsymbol{\psi}_{\mathbf{q}_0}\ .\qquad(56)$$

In terms of σ's and τ's, (56) reads

$$\begin{bmatrix}\sigma'_{\parallel}\\ \tau'_{\parallel}\\ \sigma'_{\perp}\\ \tau'_{\perp}\end{bmatrix}=\begin{bmatrix}\cos(\mathbf{q}_0\cdot\mathbf{a}) & \sin(\mathbf{q}_0\cdot\mathbf{a}) & 0 & 0\\ -\sin(\mathbf{q}_0\cdot\mathbf{a}) & \cos(\mathbf{q}_0\cdot\mathbf{a}) & 0 & 0\\ 0 & 0 & \cos(\mathbf{q}_0\cdot\mathbf{a}) & \sin(\mathbf{q}_0\cdot\mathbf{a})\\ 0 & 0 & -\sin(\mathbf{q}_0\cdot\mathbf{a}) & \cos(\mathbf{q}_0\cdot\mathbf{a})\end{bmatrix}\begin{bmatrix}\sigma_{\parallel}\\ \tau_{\parallel}\\ \sigma_{\perp}\\ \tau_{\perp}\end{bmatrix}\ .\qquad(57)$$

Because $\mathbf{q}_0$ is the reciprocal lattice vector of the $\sqrt{3}\times\sqrt{3}$ lattice, the only distinct matrices obtained from (57) are

$$\begin{bmatrix}1&0&0&0\\0&1&0&0\\0&0&1&0\\0&0&0&1\end{bmatrix},\quad\begin{bmatrix}-\frac{1}{2}&\sqrt{3}/2&0&0\\-\sqrt{3}/2&-\frac{1}{2}&0&0\\0&0&-\frac{1}{2}&\sqrt{3}/2\\0&0&-\sqrt{3}/2&-\frac{1}{2}\end{bmatrix},\quad\begin{bmatrix}-\frac{1}{2}&-\sqrt{3}/2&0&0\\ \sqrt{3}/2&-\frac{1}{2}&0&0\\0&0&-\frac{1}{2}&-\sqrt{3}/2\\0&0&\sqrt{3}/2&-\frac{1}{2}\end{bmatrix}\ .\qquad(58)$$

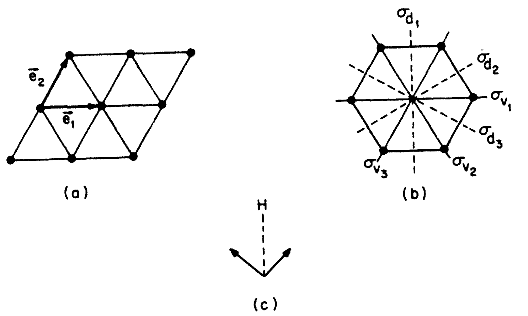

FIG. 12. Illustration of (a) translation group, (b) point group, and (c) spin-reflection group of the triangular lattice as described in the text.

Similarly, under an operation $\mathcal{R}$ of the point group, the new order parameter is the Fourier transform of the spin pattern produced by $\mathcal{R}$ (note that $\mathcal{R}$ only operates on the lattice leaving the spins fixed). Therefore,

$$\psi'_{\mathbf{q}_0}=\mathcal{R}\psi_{\mathbf{q}_0}=\sum_{\mathbf{R}} e^{-i\mathbf{q}_0\cdot\mathbf{R}}\mathbf{S}_{\mathcal{R}^{-1}\mathbf{R}}=\psi_{\mathcal{R}^{-1}\mathbf{q}_0} \; . \tag{59}$$

Since E, $2C_3$, and $3\sigma_v$ transform $\mathbf{q}_0$ into itself or points equivalent by translation by a reciprocal-lattice vector in the basis $\sigma_{\parallel}$, $\tau_{\parallel}$, $\sigma_{\perp}$, and $\tau_{\perp}$ they are represented by

$$\begin{bmatrix} 1 & 0 & 0 & 0 \\ 0 & 1 & 0 & 0 \\ 0 & 0 & 1 & 0 \\ 0 & 0 & 0 & 1 \end{bmatrix} . \tag{60}$$

The group elements C_2, $2C_6$, and $3\sigma_d$, however, map $\mathbf{q}_0$ into points equivalent to $-\mathbf{q}_0$ and are therefore represented by

$$\begin{bmatrix} 1 & 0 & 0 & 0 \\ 0 & -1 & 0 & 0 \\ 0 & 0 & 1 & 0 \\ 0 & 0 & 0 & -1 \end{bmatrix} . \tag{61}$$

Finally, under spin reflection $\psi_{\parallel}\rightarrow\psi_{\parallel}$ and $\psi_{\perp}\rightarrow-\psi_{\perp}$, so the spin-reflection group is represented by

$$\begin{bmatrix} 1 & 0 & 0 & 0 \\ 0 & 1 & 0 & 0 \\ 0 & 0 & 1 & 0 \\ 0 & 0 & 0 & 1 \end{bmatrix} \text{ and } \begin{bmatrix} 1 & 0 & 0 & 0 \\ 0 & 1 & 0 & 0 \\ 0 & 0 & -1 & 0 \\ 0 & 0 & 0 & -1 \end{bmatrix} . \tag{62}$$

The final representation of the entire group is given by multiplying the 4×4 matrices given in (58), (60)–(62). Of these, twelve are distinct. Because all the matrices are in block-diagonal form, the representation can immediately be reduced into two representations of dimension 2. The corresponding bases are simply $(\sigma_{\parallel},\tau_{\parallel})$ and $(\sigma_{\perp},\tau_{\perp})$, respectively. There are only six distinct matrices contained in the representation based on $(\sigma_{\parallel},\tau_{\parallel})$ and are given by

$$\begin{bmatrix} 1 & 0 \\ 0 & 1 \end{bmatrix}, \begin{bmatrix} -\frac{1}{2} & -\sqrt{3}/2 \\ \sqrt{3}/2 & -\frac{1}{2} \end{bmatrix}, \begin{bmatrix} -\frac{1}{2} & \sqrt{3}/2 \\ -\sqrt{3}/2 & -\frac{1}{2} \end{bmatrix},$$
$$\begin{bmatrix} 1 & 0 \\ 0 & -1 \end{bmatrix}, \begin{bmatrix} -\frac{1}{2} & -\sqrt{3}/2 \\ -\sqrt{3}/2 & \frac{1}{2} \end{bmatrix}, \begin{bmatrix} -\frac{1}{2} & \sqrt{3}/2 \\ \sqrt{3}/2 & \frac{1}{2} \end{bmatrix} . \tag{63}$$

It is straightforward to prove that these matrices are isomorphic to the point group C_{3v}, where

$$C_{3v}=\{E,2c_3,3\sigma_v\} \; . \tag{64}$$

The representation based on $(\sigma_{\perp},\tau_{\perp})$, however, is composed of twelve matrices:

$$\begin{bmatrix} 1 & 0 \\ 0 & 1 \end{bmatrix}, \begin{bmatrix} -\frac{1}{2} & -\sqrt{3}/2 \\ \sqrt{3}/2 & -\frac{1}{2} \end{bmatrix}, \begin{bmatrix} -\frac{1}{2} & \sqrt{3}/2 \\ -\sqrt{3}/2 & -\frac{1}{2} \end{bmatrix},$$
$$\begin{bmatrix} 1 & 0 \\ 0 & -1 \end{bmatrix}, \begin{bmatrix} -\frac{1}{2} & -\sqrt{3}/2 \\ -\sqrt{3}/2 & \frac{1}{2} \end{bmatrix}, \begin{bmatrix} -\frac{1}{2} & \sqrt{3}/2 \\ \sqrt{3}/2 & \frac{1}{2} \end{bmatrix},$$
$$\begin{bmatrix} -1 & 0 \\ 0 & -1 \end{bmatrix}, \begin{bmatrix} \frac{1}{2} & \sqrt{3}/2 \\ -\sqrt{3}/2 & \frac{1}{2} \end{bmatrix}, \begin{bmatrix} \frac{1}{2} & -\sqrt{3}/2 \\ \sqrt{3}/2 & \frac{1}{2} \end{bmatrix},$$
$$\begin{bmatrix} -1 & 0 \\ 0 & 1 \end{bmatrix}, \begin{bmatrix} \frac{1}{2} & \sqrt{3}/2 \\ \sqrt{3}/2 & -\frac{1}{2} \end{bmatrix}, \begin{bmatrix} \frac{1}{2} & -\sqrt{3}/2 \\ -\sqrt{3}/2 & -\frac{1}{2} \end{bmatrix}, \tag{65}$$

and is isomorphic to the group C_{6v}.

We are now in a position to consider a variety of possible transitions that may occur for this system. Rather than analyze the full range of cases, including all possible first-order phase transitions, guided by the numerical results in the next section we shall limit the range of possibilities to those that include all possible continuous transitions. Our analysis is based on the first Landau rule,[28] which states that for a continuous transition, the symmetry group of the lower-symmetry phase must be a subgroup of the symmetry group of the higher-symmetry phase. In Table I we list all possible subgroups of (52) assuming the largest periodicity is $\sqrt{3}\times\sqrt{3}$. The representations based on $(\sigma_{\parallel},\tau_{\parallel})$ and $(\sigma_{\perp},\tau_{\perp})$ for these groups are listed in the fourth column of this table. For convenience, these representations are designated in terms of the groups to which they are isomorphic. From here on we will also denote the subgroups in terms of their representation designation. The spatial symmetries of the six groups given in Table I are illustrated in Fig. 13.

In Fig. 14 we show all the possible continuous transitions (indicated by numbered arrows) between the various subgroups. Our objective in the rest of this section is to identify the form of the order parameter for each subgroup and to analyze each transition in detail, including construction of the invariant elements of the action and identification of the universality class whenever possible.

To isolate components of the order parameter which

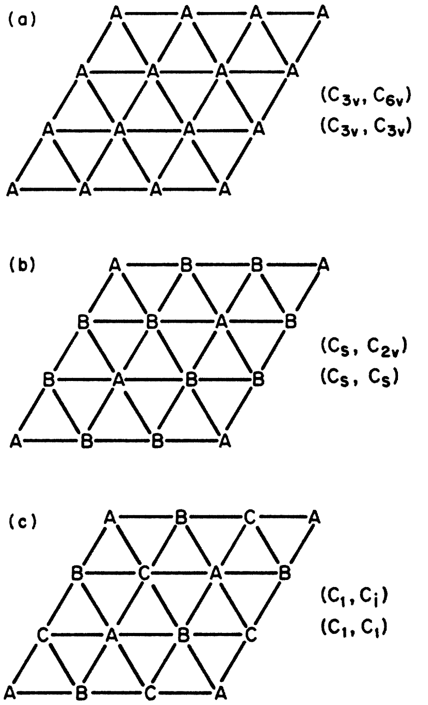

FIG. 13. Illustration of translational and point-group symmetries of the six subgroups listed in Table I. (a) (1×1) translational and C_{6v} point-group symmetry: (b) $(\sqrt{3}\times\sqrt{3})$ translational and C_{6v} point-group symmetry. (c) $(\sqrt{3}\times\sqrt{3})$ translational and C_{3v} point-group symmetry.

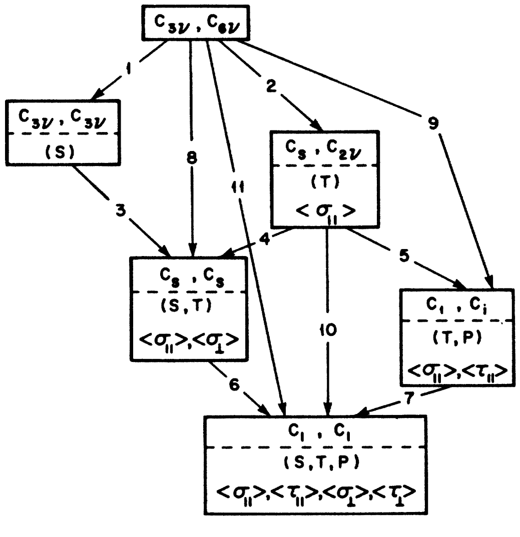

FIG. 14. All possible continuous transitions (indicated by numbered arrows) between the various subgroups given in Table I. The notation S, T, and P corresponds to the breaking of spin-group, (1×1)-translation-group, and point-group symmetries, respectively. The components of the order parameter that remain unconstrained from group-theoretical arguments are also given for each subgroup.

TABLE I. All subgroups of the space group of the AFP model on a triangular lattice in the presence of a uniform magnetic field. The representations based on $(\sigma_{\|},\tau_{\|})$ and $(\sigma_{\perp},\tau_{\perp})$ for these groups are listed in the fourth column in terms of the group to which they are isomorphic. The components of the order parameter that remain unconstrained by symmetry are given in the fifth column. The last four columns give the forms of the order parameter appropriate for each subgroup if each symmetry-breaking transition can be characterized by a new nonvanishing component of the order parameter. Question marks denote any possible value.

Spin group	Translation group	Point group	Representation	Unconstrained components	$\langle\sigma_{\|}\rangle$	$\langle\tau_{\|}\rangle$	$\langle\sigma_{\perp}\rangle$	$\langle\tau_{\perp}\rangle$
C_S	$\{m\hat{e}_1+n\hat{e}_2;\ m,n=\text{integer}\}$ $\hat{e}_1=\hat{x}\ \ \hat{e}_2=\frac{1}{2}\hat{x}+(\sqrt{3}/2)\hat{y}$	C_{6v}	(C_{3v},C_{6v})		0	0	0	0
I	$\{m\hat{e}_1+n\hat{e}_2;m,n=\text{integer}\}$	C_{6v}	(C_{3v},C_{3v})		0	0	0	0
C_S	$\{(m+2n)\hat{e}_1+(m-n)\hat{e}_2;\ m,n=\text{integer}\}$	C_{6v}	(C_s,C_{2v})	$\langle\sigma_{\|}\rangle$	$\neq0$	0	0	0
I	$\{(m+2n)\hat{e}_1+(m-n)\hat{e}_2;\ m,n=\text{integer}\}$	C_{6v}	(C_s,C_s)	$\langle\sigma_{\|}\rangle,\langle\sigma_{\perp}\rangle$	?	0	$\neq0$	0
C_S	$\{(m+2n)\hat{e}_1+(m-n)\hat{e}_2;\ m,n=\text{integer}\}$	C_{3v}	(C_1,C_i)	$\langle\sigma_{\|}\rangle,\langle\tau_{\|}\rangle$	?	$\neq0$	0	0
I	$\{(m+2n)\hat{e}_1+(m-n)\hat{e}_2;\ m,n=\text{integer}\}$	C_{3v}	(C_1,C_1)	$\langle\sigma_{\|}\rangle,\langle\tau_{\|}\rangle,\langle\sigma_{\perp}\rangle,\langle\tau_{\perp}\rangle$	?	?	?	$\neq0$
					?	$\neq0$	$\neq0$	0

may have a finite expectation value in phases characterized by each of the symmetry groups in Table I, it is convenient to use projection operators constructed from the matrices (63) and (65). For the order parameter to be invariant under each group operation, it must be the identity representation of the group. From an arbitrary function, the component corresponding to the identity representation may be projected out by evaluating the sum obtained by letting each group element act separately on the function. Thus, for an order parameter of the form $\binom{\langle\sigma\rangle}{\langle\tau\rangle}$, where for the moment $\langle\sigma\rangle$ and $\langle\tau\rangle$ represent the thermal average of either the parallel or perpendicular component, we may project out the identity representation as follows:

$$P_G\begin{bmatrix}\langle\sigma\rangle\\ \langle\tau\rangle\end{bmatrix}=\begin{bmatrix}\langle\sigma\rangle\\ \langle\tau\rangle\end{bmatrix}, \tag{66}$$

where

$$P_G=\frac{1}{h}\sum_{R\in G}\Gamma(R), \tag{67}$$

h is the order of the group, and $\Gamma(R)$ is given by one of the matrices in (63) or (65) representing the operation of the group element R on $\binom{\langle\sigma\rangle}{\langle\tau\rangle}$. If

$$P_G=\begin{bmatrix}0 & 0\\ 0 & 0\end{bmatrix},$$

then (48) has no component corresponding to the identity representation and thus $\langle\sigma\rangle=0$ and $\langle\tau\rangle=0$.

For each of the groups C_{6v}, C_{3v}, C_{2v}, and C_i, the sum over representation matrices yields

$$P_G=\begin{bmatrix}0 & 0\\ 0 & 0\end{bmatrix}$$

so that the order parameter vanishes. The group C_s contains

$$\begin{bmatrix}1 & 0\\ 0 & 1\end{bmatrix} \text{ and } \begin{bmatrix}1 & 0\\ 0 & -1\end{bmatrix}$$

so that (66) implies $\langle\tau\rangle=0$ and $\langle\sigma\rangle$ may be anything. Note, as discussed in connection with (49), that a different choice of the sublattice with respect to which $\psi_{\mathbf{q}_0}$ is defined would transform the order parameter into a solution rotated by ±120°,

$$\begin{bmatrix}\langle\sigma'\rangle\\ \langle\tau'\rangle\end{bmatrix}=\begin{bmatrix}-\frac{1}{2} & \pm\sqrt{3}/2\\ \mp\sqrt{3}/2 & -\frac{1}{2}\end{bmatrix}\begin{bmatrix}\langle\sigma\rangle\\ 0\end{bmatrix}. \tag{68}$$

For terseness in the subsequent discussion, we will always assume we have selected the sublattice for which $\langle\tau\rangle=0$, but it is clear that in numerical studies, all three cases must be considered. Finally, the group C_1 contains only the identity, so there are no restrictions on $\langle\tau\rangle$ or $\langle\sigma\rangle$. The constraints on $\langle\psi\rangle$ posed by these symmetry considerations are summarized for future reference in Table II.

TABLE II. Constraints on the order parameter for each phase arising from invariance with respect to the point-group operation.

Symmetry of phase	Constraint on $\langle\psi\rangle$
C_{6v}	$\langle\sigma\rangle=0$, $\langle\tau\rangle=0$
C_{3v}	$\langle\sigma\rangle=0$, $\langle\tau\rangle=0$
C_{2v}	$\langle\sigma\rangle=0$, $\langle\tau\rangle=0$
C_i	$\langle\sigma\rangle=0$, $\langle\tau\rangle=0$
C_s	$\langle\tau\rangle=0$
C_1	

Whereas, the preceding symmetry arguments specify components of the order parameter which must vanish, further physical information or assumptions are required to specify which of the unconstrained components are nonzero. Hence, we will assume for the present, as borne out for certain cases by the numerical results in the next section, that each symmetry-breaking transition is characterized by the emergence of a new nonvanishing component of the order parameter.

Once the components of the order parameter which become critical at a transition are determined, it is possible to construct the action describing that transition. One simply expands the action in terms of all possible products of the critical components of the order parameter which are invariant under all operations of the higher-symmetry group involved in the transition. Unfortunately, in two dimensions all symmetry-breaking terms are relevant so that this expansion cannot be truncated at any finite order. Nevertheless, it is possible to determine a set of basic building-block elements from which any allowed term in the expansion may be constructed.

If the higher-symmetry phase in a given transition is translationally invariant on the original 1×1 lattice, i.e., (1×1) translationally invariant, then a necessary condition on a term in the action is that it be composed of products of the invariant elements $\psi_\alpha\psi_\beta^*$ and/or $\psi_\alpha\psi_\beta\psi_\gamma$, where $\alpha,\beta,\gamma=||,\perp$. The corresponding building-block elements and their parities under point-group operations and spin reflections are summarized in Table III. To construct the invariants under any specific group one needs only to multiply these basic elements together so that the net parity is even.

Finally, if the higher-symmetry phase in a given transition is $(\sqrt{3}\times\sqrt{3})$ translationally invariant, then a necessary condition of the action is that it be composed of products of σ_α and/or τ_β. The basic building-block elements and their parities for this case are summarized in Table IV.

We will now proceed to apply all of the symmetry considerations discussed above to the parallel and perpendicular components of the order parameter for each transition in Fig. 14. We consider each transition in Fig. 14 in turn, in the order indicated in the figure.

1. $(C_{3v},C_{6v})\rightarrow(C_{3v},C_{3v})$

As seen in Table I and Fig. 14, this transition is associated with the breaking of spin-reflection symmetry. Since, as discussed above, both C_{6v} and C_{3v} have vanish-

TABLE III. The basic building-block elements used to construct invariants for the action for a (1×1) translationally invariant phase and their parities under point-group operations and spin reflection.

Element	(1×1) translation $\psi\rightarrow e^{i\mathbf{q}_0\cdot\mathbf{a}}\psi$	Point-group operation $\psi\rightarrow\psi^*$	Spin reflection $\psi\rightarrow(\psi_{\parallel},-\psi_{\perp})$
$\psi_{\parallel}\psi_{\parallel}^*$	+	+	+
$\psi_{\perp}\psi_{\perp}^*$	+	+	+
$\mathrm{Re}(\psi_{\parallel}\psi_{\perp}^*)$	+	+	−
$\mathrm{Im}(\psi_{\parallel}\psi_{\perp}^*)$	+	−	−
$\mathrm{Re}(\psi_{\parallel}^3)$	+	+	+
$\mathrm{Im}(\psi_{\parallel}^3)$	+	−	+
$\mathrm{Re}(\psi_{\perp}^3)$	+	+	−
$\mathrm{Im}(\psi_{\perp}^3)$	+	−	−
$\mathrm{Re}(\psi_{\parallel}^2\psi_{\perp})$	+	+	−
$\mathrm{Im}(\psi_{\parallel}^2\psi_{\perp})$	+	−	−
$\mathrm{Re}(\psi_{\parallel}\psi_{\perp}^2)$	+	+	+
$\mathrm{Im}(\psi_{\parallel}\psi_{\perp}^2)$	+	−	+

ing order parameters, both $\langle\psi_{\parallel}\rangle$ and $\langle\psi_{\perp}\rangle$ vanish before and after the transition, and the transition is not reflected in the order parameter. Physically, it is clear that the order parameter defined in (47) for $\sqrt{3}\times\sqrt{3}$ symmetry will not manifest a transition preserving 1×1 symmetry. Case 1 is the only transition for which our order parameter is irrelevant.

2. $(C_{3v},C_{6v})\rightarrow(C_s,C_{2v})$

This transition is associated with the breaking of (1×1) translational symmetries. From Table II, all components of $\langle\sigma\rangle$ and $\langle\tau\rangle$ are constrained to be 0 except for $\langle\sigma_{\parallel}\rangle$ in the symmetry-breaking phase. In order for (C_s,C_{2v}) to have a lower symmetry, we must also require that $\langle\sigma_{\parallel}\rangle\neq0$. Thus, in terms of the four-component spinor

$$\begin{bmatrix}\langle\sigma_{\parallel}\rangle\\ \langle\tau_{\parallel}\rangle\\ \langle\sigma_{\perp}\rangle\\ \langle\tau_{\perp}\rangle\end{bmatrix}$$

the transition is characterized by

$$\begin{array}{c}\langle\sigma_{\parallel}\rangle\\ \langle\tau_{\parallel}\rangle\\ \langle\sigma_{\perp}\rangle\\ \langle\tau_{\perp}\rangle\end{array}: \begin{bmatrix}0\\0\\0\\0\end{bmatrix}\rightarrow\begin{bmatrix}\neq0\\0\\0\\0\end{bmatrix}. \tag{69}$$

Since there are three different sublattice choices (68) for breaking the (1×1) translational symmetry, three different combinations of $\langle\sigma_{\parallel}\rangle$ and $\langle\tau_{\parallel}\rangle$ may become critical. Thus, in constructing the action describing this transition, one needs to write all possible products of $\psi_{\parallel}$ under the constraint that they are invariant under all operations of the higher-symmetry group, in this case C_{3v}. Since C_{3v} is (1×1) translationally invariant, we conclude from Table III that the action is constructed from invariant products of 1, $\psi_{\parallel}^*\psi_{\parallel}$, $\mathrm{Re}(\psi_{\parallel}^3)$, and $\mathrm{Im}(\psi_{\parallel}^3)$.

Furthermore, we note that the number of components in the order parameter and the symmetry which dictates this expansion are the same as that of the three-state-Potts model.[29] Thus, we conclude that this transition should be in the same universality class as the three-state-Potts model in two dimensions. This merely reflects the fact that there are three possible ways of breaking the spatial symmetry from that shown in Fig. 13(a) to that shown in Fig. 13(b).

TABLE IV. The basic building-block elements used to construct invariants for the action for a $(\sqrt{3}\times\sqrt{3})$ translationally invariant phase and their parities under point-group operations and spin reflection.

Element	$(\sqrt{3}\times\sqrt{3})$ translation	Point-group operation	Spin reflection
$\sigma_{\parallel}$	+	+	+
$\tau_{\parallel}$	+	−	+
$\sigma_{\perp}$	+	+	−
$\tau_{\perp}$	+	−	−

3. $(C_{3v},C_{3v})\rightarrow(C_s,C_s)$

This transition is also associated with the reduction of translational symmetry. Now, both the $\parallel$ and $\perp$ components undergo the transition $C_{3v}\rightarrow C_s$ analyzed in case 2, so that both $\langle\sigma_{\parallel}\rangle$ and $\langle\sigma_{\perp}\rangle$ are unconstrained. In order for (C_s,C_s) to have lower symmetry than both (C_{3v},C_{3v}) and (C_s,C_{2v}), we must require $\langle\sigma_{\perp}\rangle\neq0$ in the lower-symmetry phase, while $\langle\sigma_{\parallel}\rangle$ can have any value. Thus, the transition can be represented as follows:

$$\begin{array}{c}\langle\sigma_{\parallel}\rangle\\ \langle\tau_{\parallel}\rangle\\ \langle\sigma_{\perp}\rangle\\ \langle\tau_{\perp}\rangle\end{array}: \begin{bmatrix}0\\0\\0\\0\end{bmatrix}\rightarrow\begin{bmatrix}?\\0\\\neq0\\0\end{bmatrix}. \tag{70}$$

Recalling again that there are three sublattice choices, all the components of the order parameter may become critical. Thus, this transition is described by a four-component order parameter, and the action is constructed from products of all the elements in Table III which are invariant under the point operation.

4. $(C_s,C_{2v})\rightarrow(C_s,C_s)$

This transition is associated with the breaking of spin-reflection symmetry. From Table II we find that $\langle\tau_{\perp}\rangle$ and $\langle\tau_{\parallel}\rangle$ are constrained to be zero. As noted above, for (C_s,C_s) to have a lower symmetry, $\langle\sigma_{\perp}\rangle\neq0$ in the symmetry-breaking phase. Thus,

$$\begin{array}{c}\langle\sigma_{\parallel}\rangle\\ \langle\tau_{\parallel}\rangle\\ \langle\sigma_{\perp}\rangle\\ \langle\tau_{\perp}\rangle\end{array}: \begin{bmatrix}\neq0\\0\\0\\0\end{bmatrix}\rightarrow\begin{bmatrix}?\\0\\\neq0\\0\end{bmatrix}. \tag{71}$$

We note that although $\langle\sigma_\parallel\rangle$ may be nonzero before and after the transition, it can still change its value. At this transition both $\sigma_\parallel$ and $\sigma_\perp$ can become critical. Since C_{2v} is $\sqrt{3}\times\sqrt{3}$ translationally invariant one must use Table IV to construct the invariant products of $\sigma_\parallel$ and $\sigma_\perp$ in the expansion of the action. The *invariant* building-block elements are then given by $\sigma_\parallel$ and $\sigma_\perp^2$. The symmetry of this action is the same as that of an Ashkin-Teller[30] model in an external magnetic field.

5. $(C_s, C_{2v}) \rightarrow (C_1, C_i)$

This transition is associated with the breaking of a point-group—operation symmetry. From Table II $\langle\sigma_\perp\rangle$ and $\langle\tau_\perp\rangle$ are both constrained to be zero, whereas $\langle\sigma_\parallel\rangle$ and $\langle\tau_\parallel\rangle$ are both *unconstrained* in the lower-symmetry phase. However, if (C_1, C_i) is to have a lower symmetry, we must require $\langle\tau_\parallel\rangle\neq 0$ in the lower-symmetry phase, while $\langle\sigma_\parallel\rangle$ *unconstrained.* Thus, this transition is represented as

$$\begin{array}{c} \langle\sigma_\parallel\rangle \\ \langle\tau_\parallel\rangle \\ \langle\sigma_\perp\rangle \\ \langle\tau_\perp\rangle \end{array} : \begin{bmatrix} \neq 0 \\ 0 \\ 0 \\ 0 \end{bmatrix} \rightarrow \begin{bmatrix} ? \\ \neq 0 \\ 0 \\ 0 \end{bmatrix} . \tag{72}$$

In this case, both $\sigma_\parallel$ and $\tau_\parallel$ can become critical. From Table IV we note that the *invariant* building-block elements for the action are simply $\sigma_\parallel$ and $\tau_\parallel^2$. This action has again the same symmetry as that of an Ashkin-Teller[30] model in an external field.

6. $(C_s, C_s) \rightarrow (C_1, C_1)$

This transition is associated with the breaking of a point-group—operation symmetry. In the (C_1, C_1) phase all the components of the order parameter remain *unconstrained* from Table II. In order for (C_1, C_1) to have lower symmetry than all the other subgroups, it is evident from the last four columns of Table I that there are *two* possible conditions on the order parameter. The first is that $\langle\tau_\perp\rangle\neq 0$. The second is that $\langle\tau_\perp\rangle=0$, $\langle\sigma_\perp\rangle\neq 0$, and $\langle\tau_\parallel\rangle\neq 0$. Thus, this transition can proceed along two main channels with

7. $(C_1, C_i) \rightarrow (C_1, C_1)$

This transition is associated with the breaking of spin-reflection symmetry. It corresponds to a transition from the final state in case 5 to the final state in case 6. Thus, we may represent it as

$$\begin{array}{c} \langle\sigma_\parallel\rangle \\ \langle\tau_\parallel\rangle \\ \langle\sigma_\perp\rangle \\ \langle\tau_\perp\rangle \end{array} : \begin{bmatrix} ? \\ \neq 0 \\ 0 \\ 0 \end{bmatrix} \rightarrow \begin{bmatrix} ? \\ ? \\ ? \\ \neq 0 \end{bmatrix} \text{ or } \begin{bmatrix} ? \\ \neq 0 \\ \neq 0 \\ 0 \end{bmatrix} . \tag{74}$$

Here all the components can become critical, and from Table IV we note that the *invariant* building-block elements of the action are $\sigma_\parallel$, $\tau_\parallel$, $\sigma_\perp^2$, $\tau_\perp^2$, and $\sigma_\perp\tau_\perp$. The symmetry of the action is the same as that of case 6.

8. $(C_{3v}, C_{6v}) \rightarrow (C_s, C_s)$

From Table I we note that this transition is associated with the simultaneous breaking of spin reflection and (1×1) translational symmetries. This is a transition from the initial state of cases 1 and 2 to the final state of cases 3 and 4. Thus, we have

$$\begin{array}{c} \langle\sigma_\parallel\rangle \\ \langle\tau_\parallel\rangle \\ \langle\sigma_\perp\rangle \\ \langle\tau_\perp\rangle \end{array} : \begin{bmatrix} 0 \\ 0 \\ 0 \\ 0 \end{bmatrix} \rightarrow \begin{bmatrix} ? \\ 0 \\ \neq 0 \\ 0 \end{bmatrix} . \tag{75}$$

Allowing again all possible sublattice choices, all components of the order parameter can become critical. Thus, to construct the action all the elements in Table III must be considered. The action is then constructed out of all possible products of these elements which are invariant under both the point-group operations and spin reflection. The symmetry of this four-component model cannot be easily described, but it is expected to support a rich class of critical phenomena.

9. $(C_{3v}, C_{6v}) \rightarrow (C_1, C_i)$

This transition results from the simultaneous breaking of point-group symmetry and (1×1) transitional symmetry. We note there are six possible ways to break the symmetry as shown by considering Figs. 13(a) and 13(c). The transition is from the initial state of cases 1 and 2 to the final state of case 5. Thus, we have

10. $(C_s, C_{2v}) \rightarrow (C_1, C_1)$

This transition arises from a simultaneous breaking of spin-reflection and point-group symmetries. The transition is from the initial state of cases 4 and 5 to the final state of cases 6 and 7. Thus, we may represent it as

$$\begin{array}{c} \langle \sigma_{\parallel} \rangle \\ \langle \tau_{\parallel} \rangle \\ \langle \sigma_{\perp} \rangle \\ \langle \tau_{\perp} \rangle \end{array} : \begin{bmatrix} \neq 0 \\ 0 \\ 0 \\ 0 \end{bmatrix} \rightarrow \begin{bmatrix} ? \\ ? \\ ? \\ \neq 0 \end{bmatrix} \text{ or } \begin{bmatrix} ? \\ \neq 0 \\ \neq 0 \\ 0 \end{bmatrix} . \tag{77}$$

Here all the components of the order parameter can become critical. Since the high-symmetry phase is $\sqrt{3} \times \sqrt{3}$ translationally invariant, we must use Table IV to construct the action. We note that this action must be invariant under both spin-reflection and point-group operations. Thus, the *invariant* building-block elements are $\sigma_{\parallel}$, $\tau_{\parallel}^2$, $\sigma_{\perp}^2$, $\tau_{\perp}^2$, $\tau_{\perp}^2$, and $\tau_{\parallel}\sigma_{\perp}\tau_{\perp}$. The symmetry of this action is the same as that of an $n=4(xyzw)$ model with the x component coupled to an external field H_x and a distorted-tetrahedron corner anisotropy in the yzw space. The distortion is such that the tetrahedron fits perfectly into an orthorhombic cell.

11. $(C_{3v}, C_{6v}) \rightarrow (C_1, C_1)$

This transition is associated with the simultaneous breaking of spin-reflection, point-group, and (1×1) translational symmetries. The transition may be represented as

$$\begin{array}{c} \langle \sigma_{\parallel} \rangle \\ \langle \tau_{\parallel} \rangle \\ \langle \sigma_{\perp} \rangle \\ \langle \tau_{\perp} \rangle \end{array} : \begin{bmatrix} 0 \\ 0 \\ 0 \\ 0 \end{bmatrix} \rightarrow \begin{bmatrix} ? \\ ? \\ ? \\ \neq 0 \end{bmatrix} \text{ or } \begin{bmatrix} ? \\ \neq 0 \\ \neq 0 \\ 0 \end{bmatrix} . \tag{78}$$

Again, all components of the order parameter can become critical. The action for this transition is the same as in case 8 for $(C_{3v}, C_{6v}) \rightarrow (C_s, C_s)$. The only distinction lies in the different symmetries of the final states.

Finally, a complete analysis of all possible continuous transitions should also include transitions when no symmetry is broken. This can occur, in principle, for all the subgroups mentioned above which are characterized by an order parameter whose expectation value has at least one nonzero component. This usually will occur only at specific points in the phase diagram for continuous transitions, although it can occur along lines for first-order transitions.

This concludes the symmetry analysis for the case of nonzero external field. The results of this section will be used to analyze the numerical Monte Carlo results of the next section. Our approach will be to identify the symmetries of the higher- and lower-symmetry phases and then compare the results of critical exponents with the values predicted from the analysis in this section.

IV. MONTE CARLO SIMULATIONS

A. Monte Carlo method

We have used the standard Metropolis algorithm with each spin being updated once in each sequential sweep through the lattice. We have studied the AFP model on $L \times L$ triangular lattices with periodic boundary conditions for $L=12$, 18, 24, 36, 48, and 72. Single-spin orientations were changed with probability

$$\min(1, \exp(-\Delta E / k_B T)) ,$$

where ΔE is the energy involved in the spin reorientation. Between 2000 MCS (Monte Carlo steps per site) and 10 000 MCS were discarded to allow the system to equilibriate and then 12 000–20 000 MCS were retained for computing averages. (General features of the behavior were sometimes explored using 2000–6000 MCS.) Each data point was repeated at least once using a different random-number sequence and/or a different initial spin configuration.[31]

B. Finite-size scaling

The effect of finite lattice size on a phase transition is to smear out the behavior of the system near T_c. The properties of finite systems near the critical temperature of the corresponding infinite system can be analyzed using finite-size–scaling theory.[32,33] When the infinite system has the usual power-law singularities with critical exponents α, β, γ, ν, etc., the behavior of an $L \times L$ system can be described in terms of a reduced variable $x = tL^{1/\nu}$, where $t = |1 - T/T_c|$. Close to the infinite lattice T_c the order parameter m, the susceptibility χ, and the specific heat C are given by

$$m = L^{-\beta/\nu} f(x) , \tag{79}$$

$$\chi = L^{\gamma/\nu} g(x) , \tag{80}$$

$$C - C_0 = L^{\alpha/\nu} h(x) , \tag{81}$$

where C_0 is the nondivergent background contribution to the specific heat. Furthermore, near the infinite-lattice T_c the scaling expressions (79)–(81) must yield the usual power-law singularities as $L \rightarrow \infty$. Thus, the limiting forms as $L \rightarrow \infty$ are given by

$$f(x) \rightarrow x^{\beta} , \tag{82}$$

$$g(x) \rightarrow x^{-\gamma} , \tag{83}$$

$$h(x) \rightarrow x^{-\alpha} . \tag{84}$$

Therefore, a log-log plot of $mL^{\beta/\nu}$ versus x should have all data collapsing onto a single curve, if the values of β, ν, and T_c are correct, with asymptotic slope β. Analogous plots can be made for the other properties.

In the case of exponential singularities, the finite-size–scaling analysis can still be applied but in modified form. For example, using the Kosterlitz-Thouless form[7] with a correlation length ξ which diverges as

$$\xi = \xi_0 \exp(at^{-1/2}) , \tag{85}$$

we can rewrite the scaling expression, (80), as

$$\chi = L^{c}\tilde{g}[L^{-1}\exp(at^{-1/2})] \ . \tag{86}$$

The order parameter m goes to zero for $T < T_c$ as $L^{-\eta/2}$ with η varying with temperature. (Since the specific heat does not diverge in the Kosterlitz-Thouless description, there is no equivalent scaling form.)

Finally, we should like to end this section by noting that it has proved to be convenient, for technical reasons,[33] to use $t' = |1 - T_c/T|$ rather than t as the scaling field for $T > T_c$. It has been observed in series-expansion work[34] that for Ising-type systems (and possibly for other systems as well) one gets scaling without correction terms over a wider range by using t' instead of t.

C. General features of the phase diagram

From the behavior of the bulk properties we have been able to formulate a very rich phase diagram, which is shown in Fig. 15. Each phase is labeled by the behavior of the order parameters $\psi_{\parallel}, \psi_{\perp}$ which were defined in Sec. III B. From this diagram we see that for $H > 0$ there are four different phase boundaries separating states of different order, as well as a multicritical point, labeled A. In zero field there is a line of transitions terminating in a multicritical point where two of the finite-field phase boundaries meet. The zero-temperature transitions are known from the analysis presented in Sec. III A, and we see now that the transition for $H = 3J$, $T = 0$ is a multicritical point formed by the confluence of two finite-temperature phase boundaries.

The variation of the order parameters with field and temperature is shown in Fig. 16. The data in Fig. 16(a) clearly show that for $H = 1.5J$, $\langle \psi_{\perp} \rangle$ goes to zero at a lower temperature than $\langle \psi_{\parallel} \rangle$. (The high-temperature "tails" are purely a consequence of finite lattice size.) For $H = 5.0J$ both $\langle \psi_{\perp} \rangle$ and $\langle \psi_{\parallel} \rangle$ are nonzero at low temperature as shown in Fig. 16(b), and they both go to zero at the same temperature, albeit in a different fashion. In Fig. 16(c) we show the behavior of the order parameters as the field is swept at $k_B T = 0.4J$. All three order-order and order-disorder transitions are clearly evident.

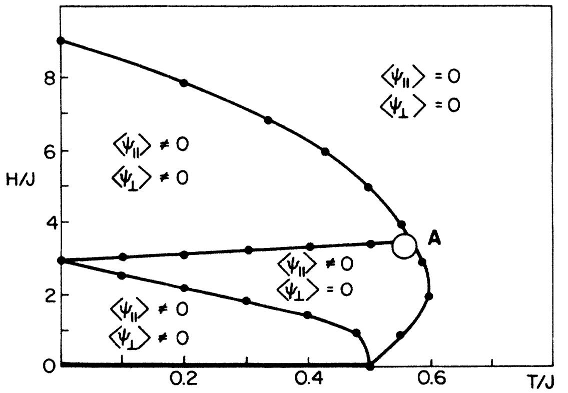

FIG. 15. Phase diagram for AFP model on a triangular lattice. Four phases can be identified and are labeled by the behavior of the order parameters $\psi_{\parallel}$ and $\psi_{\perp}$. The manner in which the three phase boundaries merge at A is not determined precisely in this work.

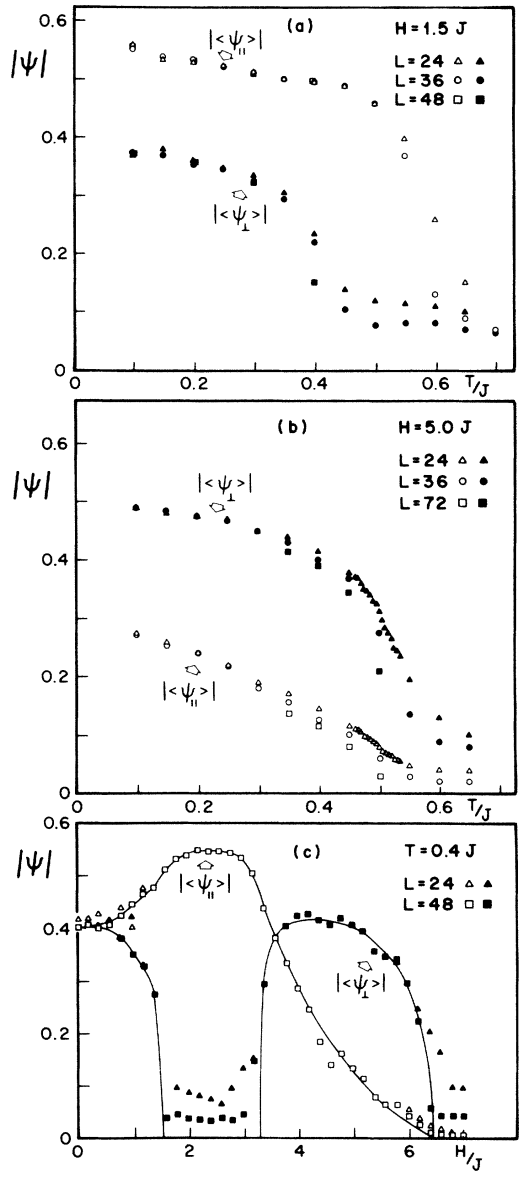

FIG. 16. Parallel and perpendicular components of the order parameter as a function of temperature and field for (a) $H = 1.5J$, (b) $H = 5.0J$, and (c) $k_B T = 0.4J$.

D. Phase transitions in zero field

We have studied the phase transition in zero magnetic field in great detail using Monte Carlo data. Typical spin patterns for three different temperatures are shown in Fig. 17. At quite low temperatures the system is ordered in a state of almost perfect staggered helicity. As the temperature is increased, elementary triangles with no helicity are increasingly abundant; however, the major change which occurs is that domains with *opposite* staggered helicity develop. The quantitative behavior of the staggered helicity and the corresponding susceptibility are shown in Fig. 18. A finite-size–scaling analysis of these data shows that the staggered helicity goes to zero at the same tem-

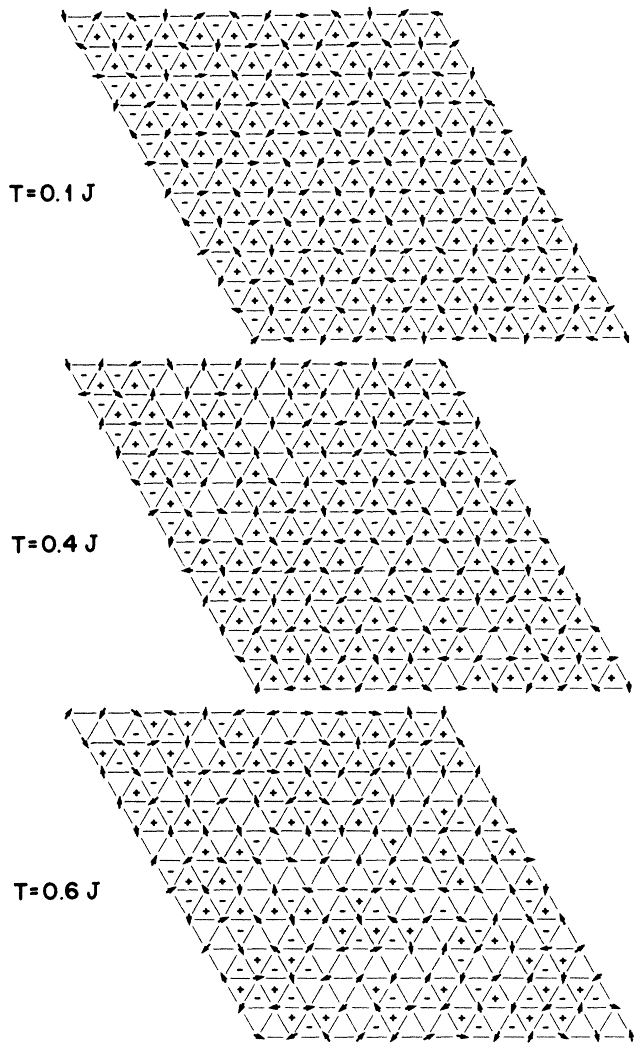

FIG. 17. Typical spin patterns for helicities for each triangle for three different temperatures as obtained from Monte Carlo simulations. Note the dramatic change in staggered helicity from $k_BT=0.4J$ to $k_BT=0.6J$.

perature, $k_BT_c=(0.510\pm0.005)J$, at which the staggered helicity susceptibility diverges and that the behavior of both are described well by two-dimensional Ising exponents. This estimate for T_c is higher than that which we had obtained from our preliminary results.[15] We now have improved data, particularly for the larger lattice sizes, and the finite-size–scaling analysis leaves no doubt that our earlier estimate was too low.

In addition to the formation of domains, we find direct evidence for the formation of bound vortex pairs. In Fig. 19(a) we show a spin configuration obtained from Monte Carlo simulations at $k_BT=0.4J$. In Fig. 19(b) we show the corresponding pattern in the orientational order parameter defined in (43). In the mapped configuration we see features reminiscent of a bound vortex-antivortex pair in addition to spin-wave excitations. These excitations destroy any low-temperature long-range spin order. We find, however, that the high-temperature orientational order susceptibility diverges exponentially fast as T_c is approached from above. A finite-size–scaling analysis, shown in Fig. 20, confirms the behavior described by (86) with $k_BT_c=(0.505\pm0.005)J$, which is the same (within our error bars) as that obtained from the analysis of the staggered helicity.

Data for the specific heat are presented in Fig. 21. Only a single peak is seen, and the peak grows and sharpens substantially as the lattice size increases. In Fig. 22 we plot the maximum value of the specific heat $C_{\max}$ versus $\ln L$. The data are consistent with a linear increase with $\ln L$ and, hence, with a logarithmic divergence of the specific heat for the infinite lattice. (It is worth noting that Miyashita and Shiba[16] found a logarithmic divergence of $C_{\max}$ with L for the 36-state clock model, but their values are systematically higher than ours for $L\geq 18$.)

Lastly, we have determined the behavior of the spin-wave–stiffness constant which was defined in Eqs. (39) and (40). Our results, which are shown in Fig. 23, show substantial finite-size effects in the region near and above

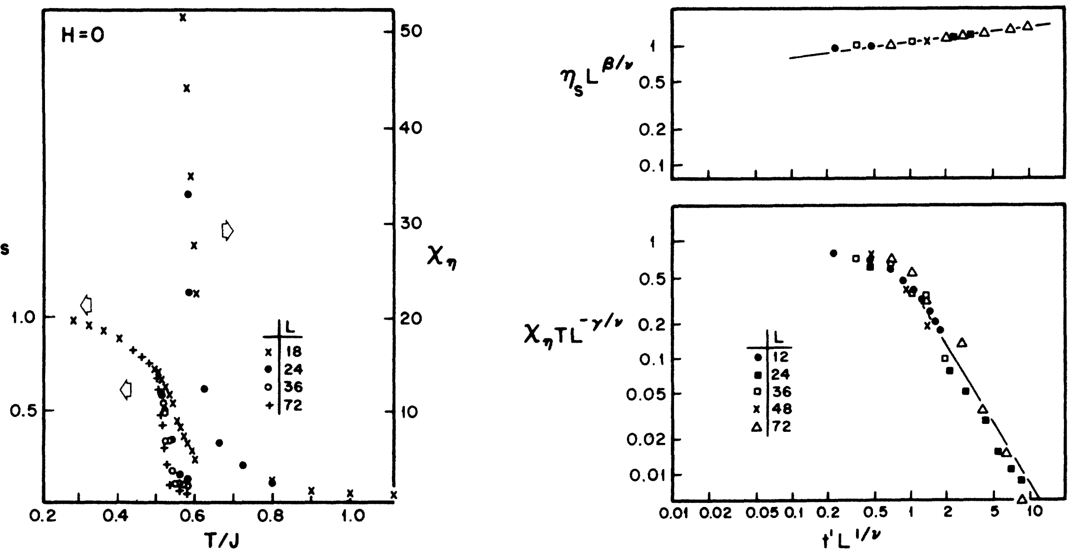

FIG. 18. Staggered helicity and corresponding susceptibility as a function of temperature (left). Finite-size–scaling analysis (right).

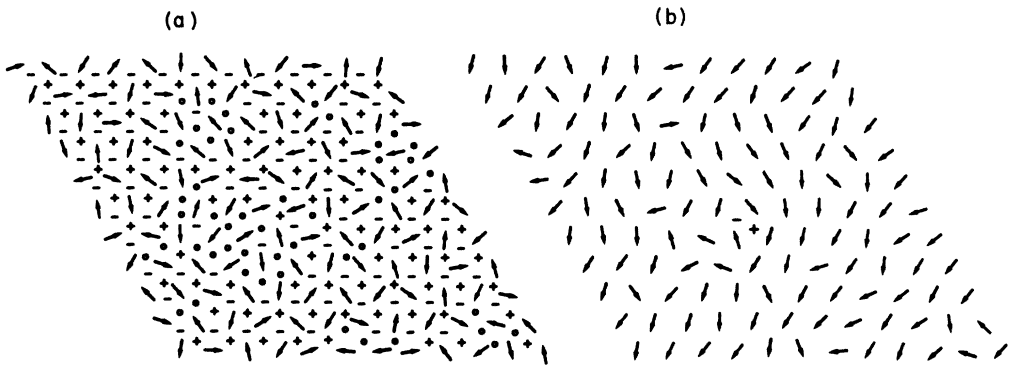

FIG. 19. (a) Spin configuration obtained from Monte Carlo simulations at $k_BT=0.4J$ and $H=0$. (b) Corresponding pattern in the orientational order parameter defined in Eq. (43) in the text. Note the presence of a bound vortex-antivortex pair in addition to spin-wave excitations.

T_c. Using the range of values of $k_BT_c=(0.505\text{—}0.510)J$ determined previously, we conclude that the value of the spin-wave—stiffness constant at T_c is *consistent* with the universal jump[20]

$$\lim_{T\to T_c}[\gamma(T)/k_BT]=2/\pi\ . \tag{87}$$

Our results, thus, suggest that there is a single phase transition which has both Ising and xy character as far as the critical behavior of different bulk properties is concerned.

E. Phase transitions in nonzero field

As we have already shown in Fig. 15, the application of a uniform magnetic field produces a very rich phase diagram. In order to clearly identify the nature of the various phase boundaries and their relationship to the transitions permitted by symmetry (see Fig. 14), we first examine the behavior of the order parameters σ,τ which were defined in Eqs. (48) and (49). Note that in spite of the threefold ambiguity in sublattice choice reflected in (68), one can uniquely distinguish between $\langle\tau\rangle=0$, $\langle\sigma\rangle\neq0$ and $\langle\tau\rangle\neq0$, $\langle\sigma\rangle=0$. In Figs. 24(a) and 24(b) we show the magnetic field dependence of the order-parameter components as a function of temperature. At small fields ($H=1.5J$) and low temperature the system is ordered in a state with $\langle\sigma_\parallel\rangle\neq0$ and $\langle\tau_\perp\rangle\neq0$. From Table I we see then that the low-temperature, low-field state has the symmetry (C_1,C_1). As the temperature is increased, the $\langle\tau_\perp\rangle$ component goes to zero (near $k_BT=0.4J$) but $\langle\sigma_\parallel\rangle$ remains nonzero. From Table I and Fig. 14 we deduce that the symmetry of this new phase is (C_s,C_{2v}). As the temperature is increased further, $\langle\sigma_\parallel\rangle$ also disappears,

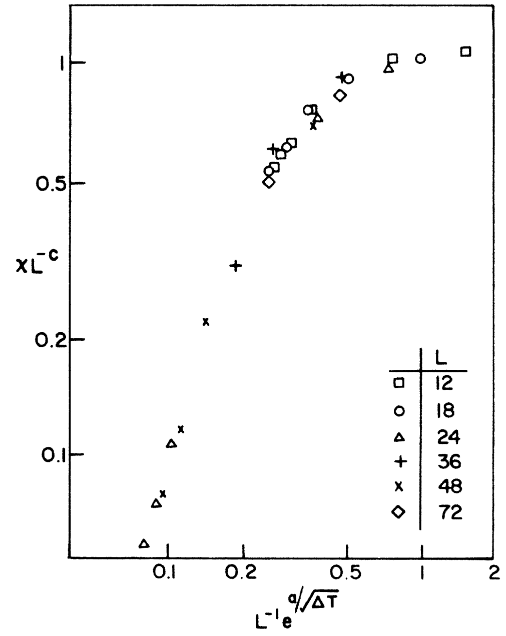

FIG. 20. Scaling analysis for orientational order susceptibility with $a=0.50$ and $c=1.70$ at zero magnetic field.

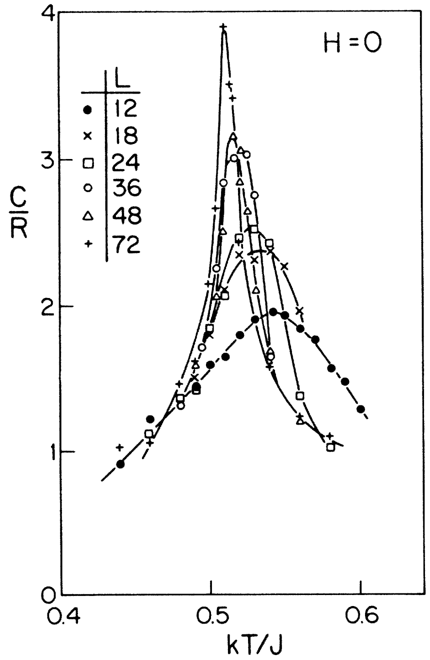

FIG. 21. Specific heat as a function of temperature for zero magnetic field.

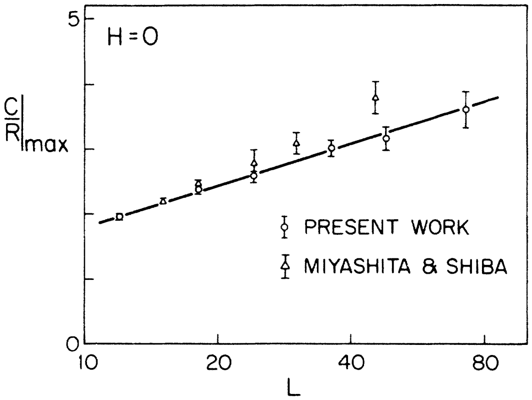

FIG. 22. Maximum of specific heat as a function of lattice size as compared with results of Ref. 16. The present data are consistent with a logarithmic divergence of $C_{\max}$ for the infinite lattice.

signaling a transition to a state with no order. (The high-temperature tails are purely a finite-size effect.) From Table I and Fig. 14, we find that this transition corresponds to $(C_s, C_{2v}) \rightarrow (C_{3v}, C_{6v})$. At high field (e.g.,

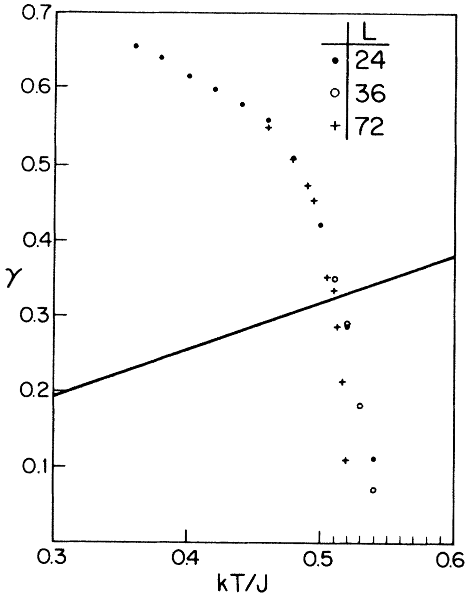

FIG. 23. Spin-wave–stiffness constant as a function of temperature. The solid line represents the function $2k_BT/\pi J$.

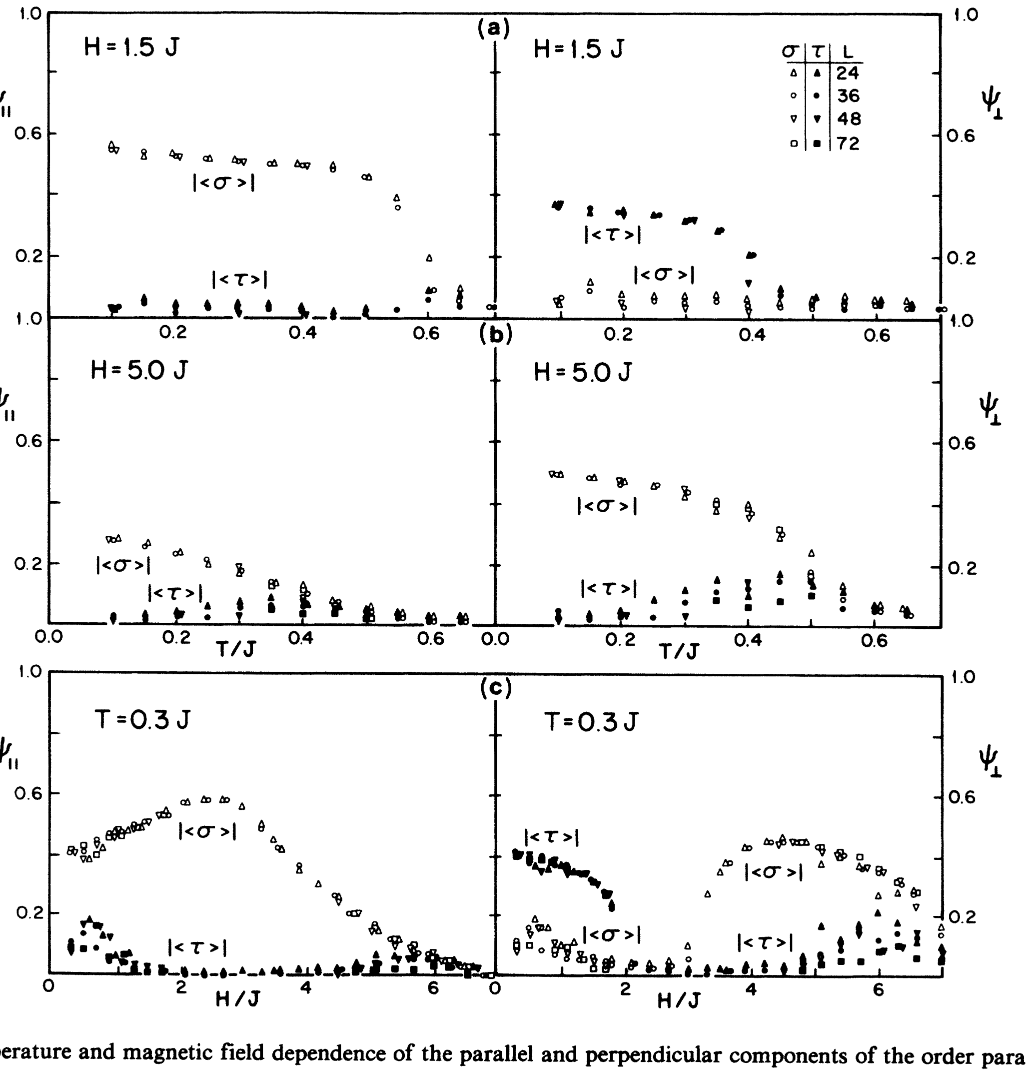

FIG. 24. Temperature and magnetic field dependence of the parallel and perpendicular components of the order parameter for (a) $H = 1.5J$, (b) $H = 5.0J$, and (c) $k_BT = 0.3J$.

$H=5.0J$), as shown in Fig. 24(b), there is a low-temperature ordered phase with $\langle\sigma_{\parallel}\rangle\neq 0$, $\langle\sigma_{\perp}\rangle\neq 0$. From Table I we conclude that this phase is (C_s,C_s). All these results are summarized in Fig. 25. We have also obtained data for $k_BT-0.3J$ as a function of field. From Fig. 25 we see that such a sweep should cut through all three ordered phases. The data, shown in Fig. 24(c), clearly shows the transitions which we have just described. (The effects of finite lattice size are quite small on the components which are clearly nonzero.) Where the finite-size effects are important they strongly suggest that the components in question extrapolate to zero for $L\rightarrow\infty$.

The qualitative behavior of the order-parameter components together with the invariant subgroup flow-chart enable us to conclude what the nature of the transitions should be. We have also studied the critical behavior along each phase boundary and can compare our observations with the theoretical predictions. In Fig. 26 we show finite-size—scaling plots for $H=2.0J$ and $H=3.0J$ showing the $(C_{3v},C_{6v})\rightarrow(C_s,C_{2v})$ transition. These plots have been made using exponents for the three-state-Potts model[29] and show excellent scaling properties: $\beta=\frac{1}{9}$, $\gamma=\frac{13}{9}$, $\nu=\frac{5}{6}$. This transition is predicted to be in the same universality class as the three-state-Potts model and our data confirm this. As shown in Fig. 27, the specific-heat maxima increase with lattice size as $L^{\alpha/\nu}$, with $\alpha=\frac{1}{3}$, $\nu=\frac{5}{6}$, as expected for the three-state-Potts model.

The character of the high-field transition $(C_{3v},C_{6v})\rightarrow(C_s,C_s)$ is completely different. Finite-size—scaling plots, see Fig. 28, show that the critical behavior is *nonuniversal.* Setting $\nu=1$ we deduce that at $H=4.0J$, $\beta=0.20$ and $\gamma=1.55$, while at $k_BT=0.3J$, $\beta=0.28$ and $\gamma=1.45$. The specific heat shows clear peaks at the transition. However, according to the dependence of the specific-heat maxima on L, shown in Fig. 29, the specific-heat peak does not diverge as $L\rightarrow\infty$. This indicates that $\alpha<0$.

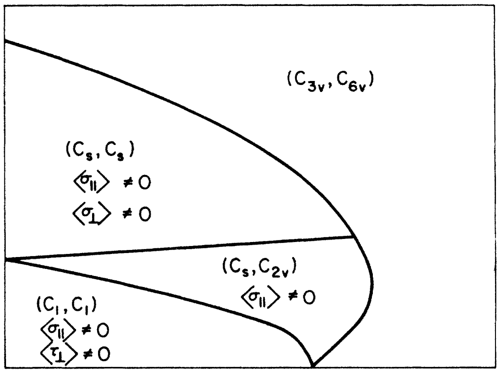

FIG. 25. Identification of the symmetries of the four phases obtained in Fig. 15.

In Fig. 30 we show results at constant temperature as the field is swept through the $(C_1,C_1)\rightarrow(C_s,C_{2v})$ transition. Here, too, the phase boundary is nonuniversal. The scaling analysis indicates $\beta=0.22$ at $k_BT=0.3J$ and $\beta=0.14$ at $k_BT=0.4J$. The specific heat also shows peaks, but these clearly do not diverge as $L\rightarrow\infty$.

Data for fixed temperature with the field swept through the $(C_s,C_{2v})\rightarrow(C_s,C_s)$ transition are shown in Fig. 31. We see that this boundary is also nonuniversal. The finite-size—scaling analysis gives $\beta=0.21$ $k_BT=0.3J$ and $\beta=0.14$ at $k_BT=0.4J$. It is particularly interesting that there is no indication of a peak in the specific heat (or a singularity in the uniform magnetization) at the phase transition and that it is only through the observation of

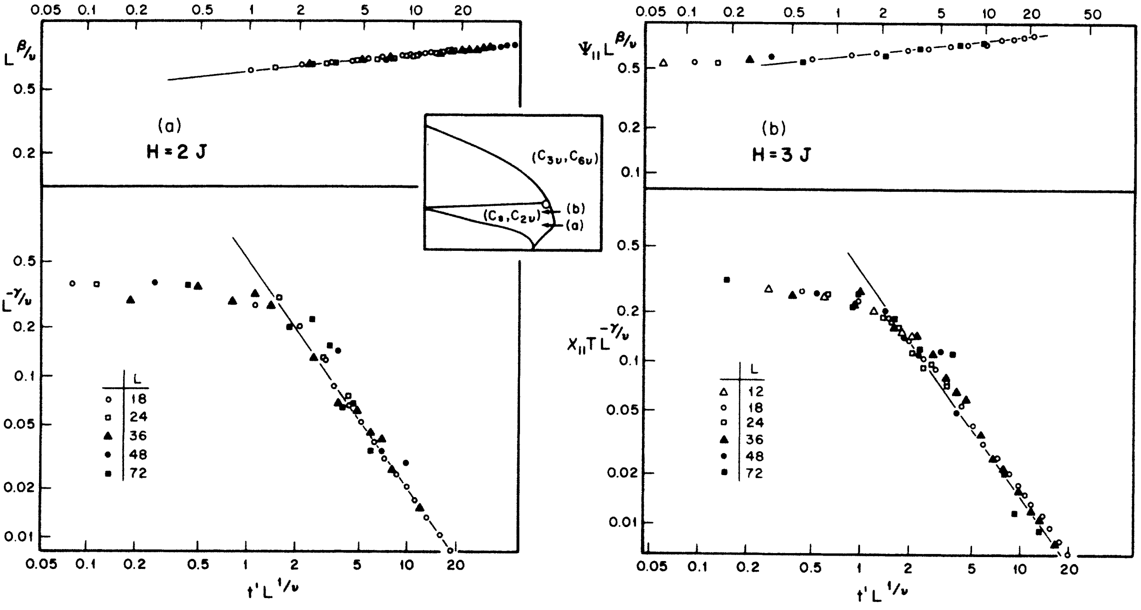

FIG. 26. Finite-size—scaling analysis for the $(C_{3v},C_{6v})\rightarrow(C_s,C_{2v})$ transition for (a) $H=2J$ and (b) $H=3J$. The plots are obtained using the exponents of a three-state-Potts model with $\beta=\frac{1}{9}$, $\gamma=\frac{13}{9}$, and $\nu=\frac{5}{6}$.

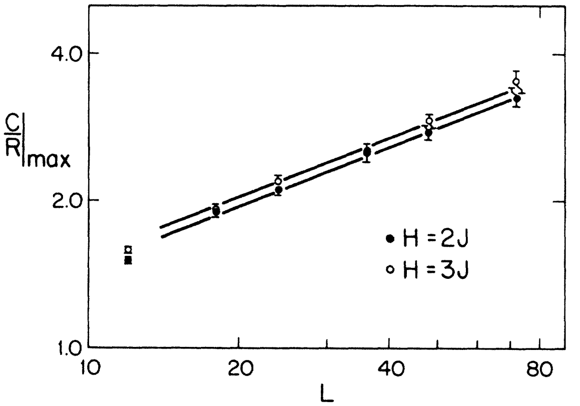

FIG. 27. Maximum of specific heat as a function of lattice size for the $(C_{3v},C_{6v})\rightarrow(C_s,C_{2v})$ transition. The exponent deduced from these results is consistent with a three-state-Potts model.

the behavior of *properly defined* order parameters that we can locate the phase transition.

V. SUMMARY AND CONCLUDING REMARKS

We have presented a detailed investigation of the AFP model on a triangular lattice using an approach which combines the rigor of group-theoretical arguments with the power of Monte Carlo simulations. This combination has proved to be essential to the correct elucidation of the entire phase diagram. Our analysis has resulted in a surprisingly rich phase supporting a variety of new critical phenomena.

One of the most interesting features is the possible existence of a multicritical point describing the confluence of the Ising and Kosterlitz-Thouless universality classes. Our results are consistent with, but do not rigorously prove, that this multicritical point actually occurs at $H=0$ near $k_BT=0.5J$. One indication suggesting the existence of only one critical point at $H=0$ is given by the results in Fig. 32. Here we present specific-heat data in the vicinity of $k_BT=0.5J$ for various values of the magnetic field. The lattice size is 72×72. Two well-defined peaks are clearly distinguishable which seem to merge into one peak as $H\rightarrow0$. The most quantitative evidence is provided by the finite-size—scaling results for the stagered helicity and spin-orientation order parameter which specify a Kosterlitz-Thouless transition at $k_BT=(0.505\pm0.005)J$ and an Ising transition at $k_BT=(0.510\pm0.005)J$. These are statistically consistent with a single multicritical point.

This analysis, however, does not rule out the possibility of the existence of two distinct transition temperatures. In this case on physical grounds $T_{\mathrm{KT}}<T_I$. Moreover, from the finite-size—scaling analysis they are within $0.01J$ of each other. Finally, it is important to note that in this system the presence of domain-wall excitations provides a physical mechanism for the two transitions to be so close and occur at low temperatures. This can be illustrated by the following heuristic argument.

Domain-wall fluctuations are present on a length scale smaller than the Ising correlation length. Consider the system at a temperature near the Kosterlitz-Thouless transition. One can now imagine integrating out the

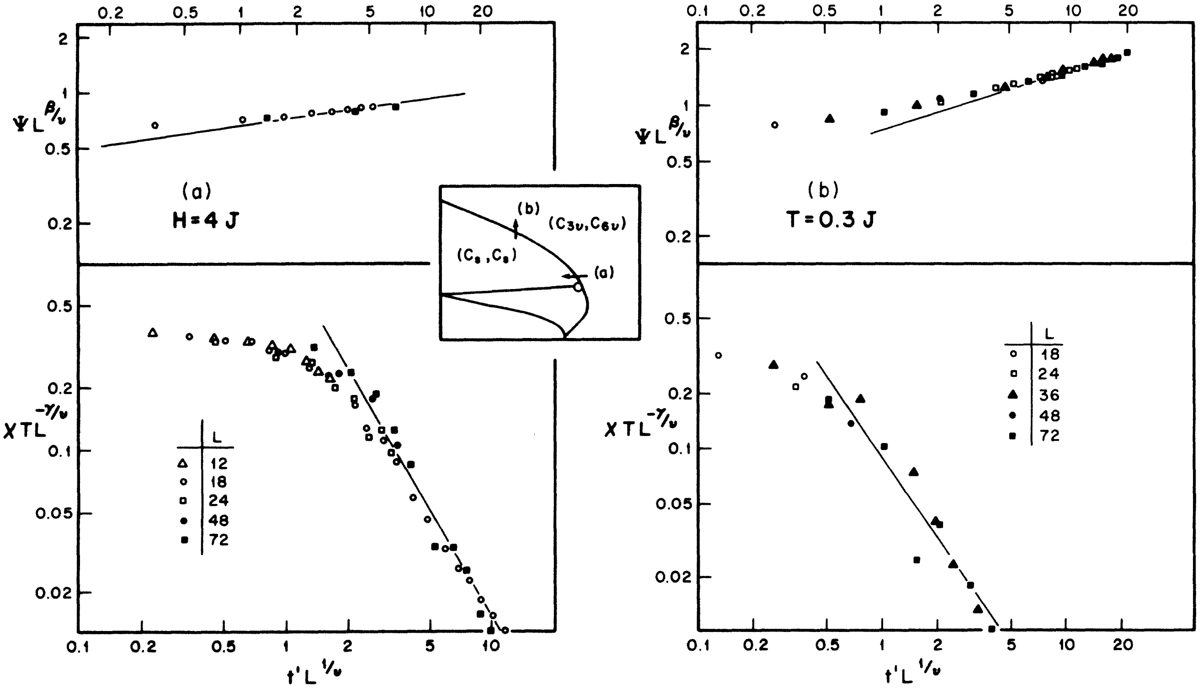

FIG. 28. Finite-size—scaling analysis for the $(C_{3v},C_{6v})\rightarrow(C_s,C_s)$ transition for (a) $H=4J$ with $\beta=0.20$, $\gamma=1.55$, and $\nu=1.0$, and (b) $k_BT=0.3J$ with $\beta=0.28$, $\gamma=1.45$, and $\nu=1.0$.

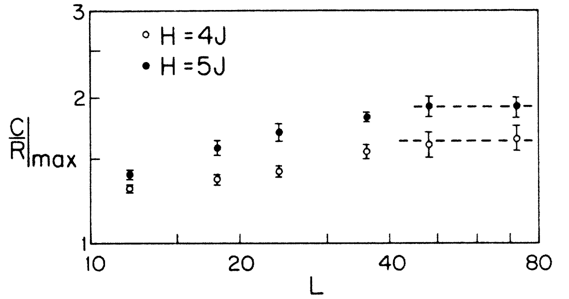

FIG. 29. Maximum of specific heat as a function of lattice size for the $(C_{3v},C_{6v})\rightarrow(C_s,C_s)$ transition. The specific heat does not appear to diverge as $L\rightarrow\infty$.

domain-wall degrees of freedom by performing coarse graining up to a length scale equal to the Ising correlation length. The net effect is to reduce the problem to a "pure" Kosterlitz-Thouless system with a *smaller* bare coupling constant J'. The vortex-antivortex—unbinding transition will now be proportional to J' and will consequently occur at a *lower* temperature than for a system which cannot support domain-wall excitations. Thus, it also follows that the closer the Ising and Kosterlitz-Thouless transitions occur, the more effective this lowering in temperature becomes. We believe that the proximity (if not coincidence) and low values of T_c are a manifestation of this effect.

Finally, it is appropriate to note that the possibility of two distinct phase transitions has been emphasized by Miyashita and Shiba.[16] Their order-disorder transition (corresponding to our T_I) is estimated two ways, yielding 0.515 ± 0.005 and 0.513 while T_{KT} is calculated to be 0.502 ± 0.002. At the standard-deviation level their temperatures are distinct (although they overlap our values of T_I and T_{KT} within error bars). The present level of numerical calculations cannot give a definite answer to the question of one or two transitions. Very recently, however, renormalization-group calculations[35] for the uniformly fully frustrated square lattice indicate the possibility of *one* nonuniversal transition consistent with our conjecture. More work is certainly needed to completely settle this issue.

ACKNOWLEDGMENTS

This work was supported in part by U.S. Office of Naval Research Grant No. N00014-770-C-0132, National Science Foundation Grant No. DMR-83-000754, and U.S. Department of Energy (DOE) Contract No. DE-AC02-76ER03069. One of us (D.H.L.) would like to thank the Program in Simulation Physics at the University of Georgia for its hospitality.

APPENDIX A

In this appendix we will derive (40) for the spin-stiffness constant γ. We recall that

$$\gamma=2\frac{\rho}{N^2}\lim_{\Delta\to 0}\left[\frac{F_b-F_a}{\Delta^2}\right]. \tag{A1}$$

Here F_a and F_b are free energies given by

$$F_a=-k_BT\ln\left\{\mathrm{Tr}^{(a)}_{\{\theta\}}\left[\exp\left[-\beta J\sum_{\langle ij\rangle}\cos(\theta_i-\theta_j)\right]\right]\right\}, \tag{A2a}$$

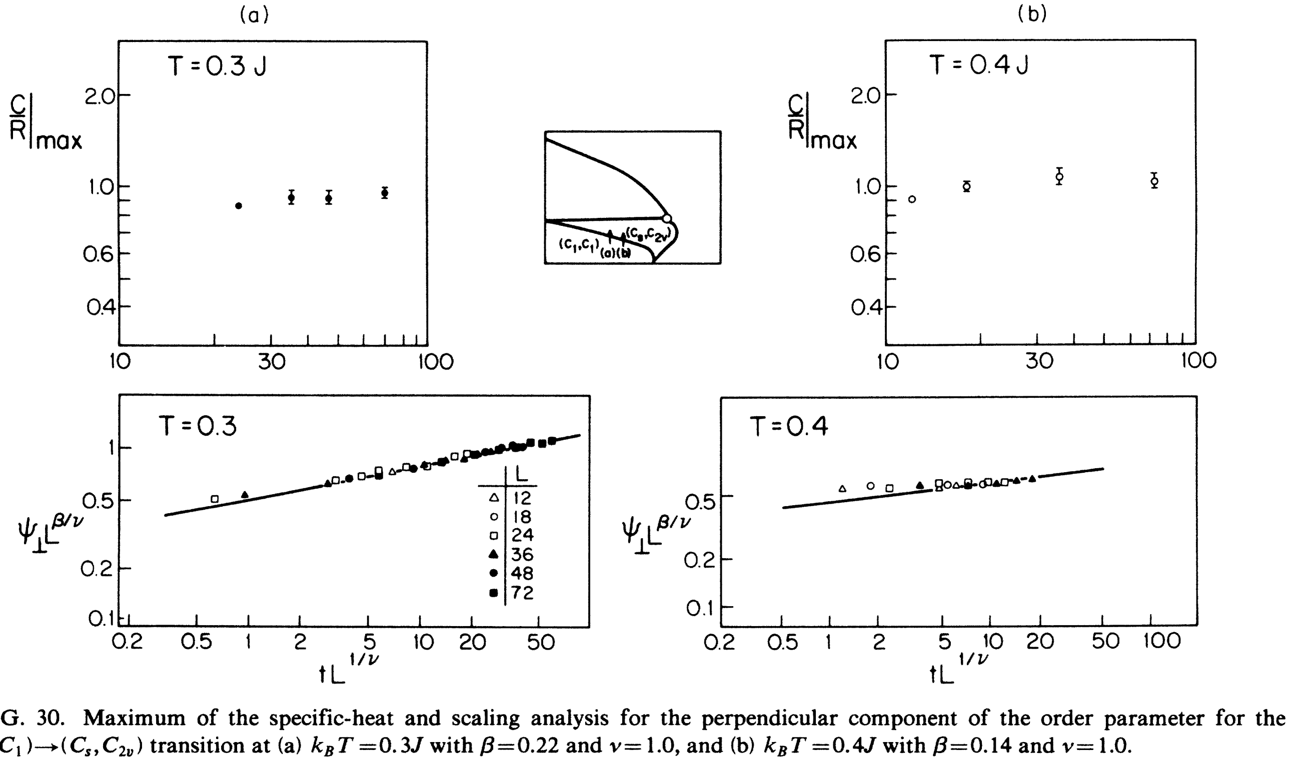

FIG. 30. Maximum of the specific-heat and scaling analysis for the perpendicular component of the order parameter for the $(C_1,C_1)\rightarrow(C_s,C_{2v})$ transition at (a) $k_BT=0.3J$ with $\beta=0.22$ and $\nu=1.0$, and (b) $k_BT=0.4J$ with $\beta=0.14$ and $\nu=1.0$.

$$F_b=-k_BT\ln\Bigg\{\mathrm{Tr}^{(b)}_{\{\theta\}}\Bigg[\exp\Bigg[-\beta J\sum_{\langle ij\rangle}\cos(\theta_i-\theta_j\Bigg]\Bigg]\Bigg\}\,, \tag{A2b}$$

where $\mathrm{Tr}^{(a)}_{\{\theta\}}$ and $\mathrm{Tr}^{(b)}_{\{\theta\}}$ designate the sum over all possible spin configurations under the boundary conditions (a) and (b) given by Eqs. (37) and (38), respectively. The key step in deriving (40) is a simple change of variables. Let us define

$$\theta'(\mathbf{r})=\theta(\mathbf{r})+\hat{\mathbf{e}}_1\cdot\mathbf{r}\Delta \tag{A3}$$

in terms of θ'. Boundary condition (b) becomes

$$\begin{aligned}\theta'(\mathbf{r}+N\hat{\mathbf{e}}_1)&=\theta'(\mathbf{r})\,,\\ \theta'(\mathbf{r}+N\hat{\mathbf{e}}_2)&=\theta'(\mathbf{r})\,,\end{aligned} \tag{A4}$$

which is exactly boundary condition (a). Therefore,

$$F_b=-k_BT\ln\Bigg\{\mathrm{Tr}^{(a)}_{\{\theta'\}}\Bigg[\exp\Bigg[-\beta J\sum_{\langle ij\rangle}\cos[\theta_i'-\theta_j'+(\hat{\mathbf{e}}_{ij}\cdot\hat{\mathbf{e}}_1)\Delta]\Bigg]\Bigg]\Bigg\}\,. \tag{A5}$$

Here $\hat{\mathbf{e}}_{ij}$ is the unit vector pointing from site j to i. Substituting (A2a) and (A5) into (A1), we obtain

$$\gamma=\frac{\rho}{N^2}\frac{\partial^2}{\partial\Delta^2}\bigg|_{\Delta=0}[-k_BT\ln(\mathrm{Tr}^{(a)}_{\{\theta\}}e^{-\beta H(\{\theta\},\Delta)})]\,, \tag{A6}$$

where

$$H(\{\theta\},\Delta)\equiv J\sum_{\langle ij\rangle}\cos[\theta_i-\theta_j+(\hat{\mathbf{e}}_{ij}\cdot\hat{\mathbf{e}}_1)\Delta]\,. \tag{A7}$$

After performing the derivatives in (A6), we obtain

$$\begin{aligned}\gamma=-k_BT\frac{\rho}{N^2}\Bigg[&\left[\frac{1}{k_BT}\right]^2\left\langle\left[\frac{\partial H}{\partial\Delta}\right]^2_{\Delta=0}\right\rangle\\ &-\frac{1}{k_BT}\left\langle\left[\frac{\partial^2 H}{\partial\Delta^2}\right]_{\Delta=0}\right\rangle\\ &-\left[\frac{1}{k_BT}\right]^2\left\langle\left[\frac{\partial H}{\partial\Delta}\right]_{\Delta=0}\right\rangle^2\Bigg]\,,\end{aligned} \tag{A8}$$

where

$$\langle O\rangle\equiv\frac{\mathrm{Tr}^{(a)}_{\{\theta\}}\left[O\exp\left[\beta J\sum_{\langle ij\rangle}\cos(\theta_i-\theta_j)\right]\right]}{\mathrm{Tr}^{(a)}_{\{\theta\}}\left[\exp\left[\beta J\sum_{\langle ij\rangle}\cos(\theta_i-\theta_j)\right]\right]}\,. \tag{A9}$$

Because $\cos(\theta_i-\theta_j)$ is even under interchange of i and j, $\langle(\partial H/\partial\Delta)_{\Delta=0}\rangle=0$. Substituting (A7) into (A8), we obtain

$$\begin{aligned}\gamma=\frac{\rho}{N^2}\Bigg[&\left\langle-J\sum_{\langle ij\rangle}(\hat{\mathbf{e}}_1\cdot\hat{\mathbf{e}}_{ij})^2\cos(\theta_i-\theta_j)\right\rangle\\ &-\frac{1}{k_BT}\left\langle\left[\sum_{\langle ij\rangle}(\hat{\mathbf{e}}_1\cdot\hat{\mathbf{e}}_{ij})\sin(\theta_i-\theta_j)\right]^2\right\rangle\Bigg]\,,\end{aligned} \tag{A10}$$

since $\rho=2/\sqrt{3}$ and $(\hat{\mathbf{e}}_1\cdot\hat{\mathbf{e}}_{ij})=1$ or $\pm\frac{1}{2}$. We obtain finally

$$\begin{aligned}\gamma=-\frac{1}{\sqrt{3}}\langle u\rangle-\frac{2}{\sqrt{3}}\frac{J^2}{k_BTN^2}&\\ \times\left\langle\left[\sum_{\langle ij\rangle}(\hat{\mathbf{e}}_1\cdot\hat{\mathbf{e}}_{ij})\sin(\theta_1-\theta_j)\right]^2\right\rangle&\,.\end{aligned} \tag{A11}$$

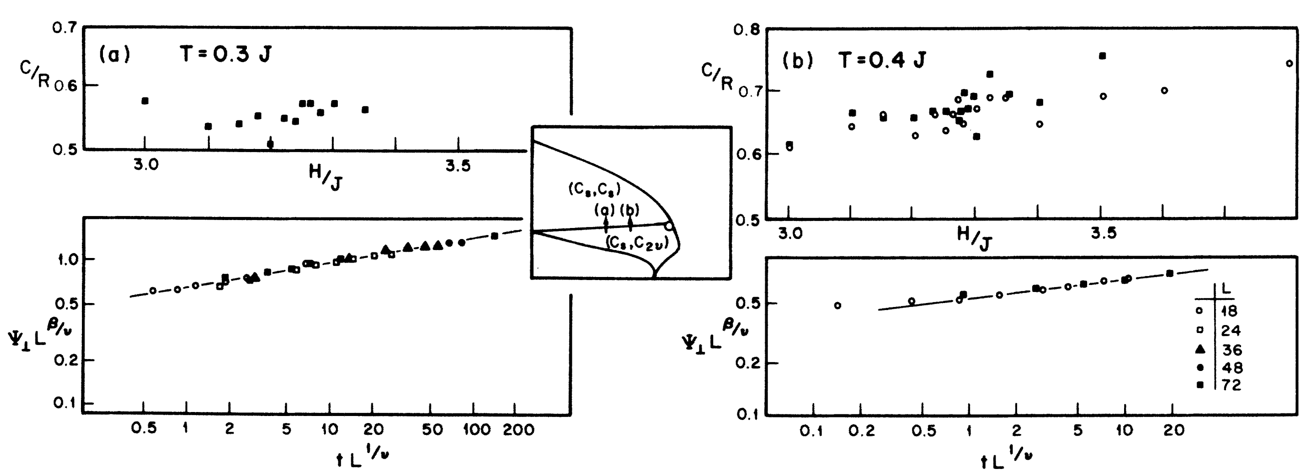

FIG. 31. Specific-heat and finite-size–scaling analysis for the perpendicular component of the order parameter for the $(C_s,C_{2v})\rightarrow(C_s,C_s)$ transition at (a) $k_BT=0.3J$ with $\beta=0.21$ and $\nu=1.0$, and (b) $k_BT=0.4J$ with $\beta=0.14$ and $\nu=1.0$. Note that there is no indication of a peak in the specific heat across the transition.

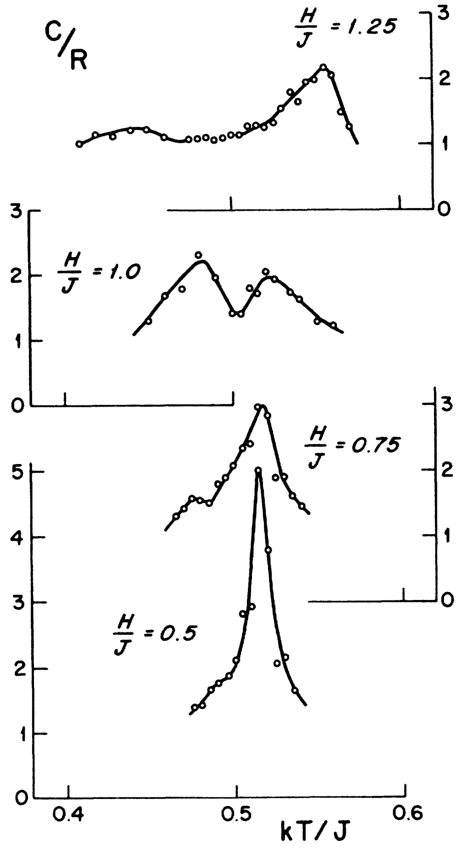

FIG. 32. Specific heat near $k_B T = 0.5J$ for various values of the magnetization. Two well-defined peaks appear to be merging into one peak as $H \to 0$. The results are for a lattice of size 72×72.

APPENDIX B

In this appendix we present proof that, even in the presence of a uniform magnetic field, the ground states of (45) exhibit a $\sqrt{3} \times \sqrt{3}$ periodicity and that the three sublattice magnetizations $\mathbf{m}_1$, $\mathbf{m}_2$, and $\mathbf{m}_3$ must satisfy

$$\mathbf{m}_1 + \mathbf{m}_2 + \mathbf{m}_3 = \frac{\mathbf{H}}{3J} \quad \text{for } H \le 9J \; . \tag{B1}$$

We first consider any elementary triangle in the triangular lattice. We label the three vertices of the triangle 1, 2, and 3. The energy of the triangle is then

$$E_\Delta = \frac{J}{2}(\mathbf{S}_1 \cdot \mathbf{S}_2 + \mathbf{S}_1 \cdot \mathbf{S}_3 + \mathbf{S}_2 \cdot \mathbf{S}_3) - \frac{\mathbf{H}}{6} \cdot (\mathbf{S}_1 + \mathbf{S}_2 + \mathbf{S}_3) \; . \tag{B2}$$

The weighting factors of $\frac{1}{2}$ and $\frac{1}{6}$ are defined such that the total energy of the triangular lattice is obtained by summing E_Δ over all elementary triangles.

Thus, the ground-state energy E_G of the entire triangular lattice must satisfy

$$E_G \ge \sum_\Delta E_\Delta^G \; , \tag{B3}$$

where E_Δ^G is the ground-state energy of (B2). If we can now show that each elementary triangle can realize its ground-state pattern on the triangular lattice as a whole, the equality in (B3) holds, and this state must be a ground state. Moreover, it then follows from (B3) that any other ground state of the triangular lattice must also have each elementary triangle in one of its ground states, since if a Δ were not in its ground state, the equality in (B3) would be violated.

To calculate the ground state of an elementary triangle, we rewrite (B2) as

$$\frac{E_\Delta}{J} = -\frac{1}{4}\left[3 + \frac{H^2}{9J^2}\right] + \frac{1}{4}\left[\mathbf{S}_1 + \mathbf{S}_2 + \mathbf{S}_3 - \frac{\mathbf{H}}{3J}\right]^2 . \tag{B4}$$

It is now clear that for $H \le 9J$ the minimum of (B4) is realized when

$$\mathbf{S}_1 + \mathbf{S}_2 + \mathbf{S}_3 = \frac{\mathbf{H}}{3J} \; , \tag{B5}$$

and for $H > 9J$ the appropriate solution is

$$\mathbf{S}_1 = \mathbf{S}_2 = \mathbf{S}_3 = \hat{\mathbf{H}} \; . \tag{B6}$$

The elementary-triangle ground-state pattern (B5) can be used to construct a ground state in the triangle lattice in the following way. One simply begins with one elementary triangle in one of its ground states. Since any two spins on the edge of an elementary triangle generates a third spin using constraint (B5), this procedure specifies all the spins on all the other lattice sites of the system. The resulting spin configuration is a ground state for the triangular lattice and is forced from (B5) to be $\sqrt{3} \times \sqrt{3}$.

---

*Present address: IBM Thomas J. Watson Research Center, Yorktown Heights, NY 10598.

[1] N. D. Mermin and H. Wagner, Phys. Rev. Lett. **22**, 1133 (1966).
[2] H. E. Stanley and T. A. Kaplan, Phys. Rev. Lett. **17**, 913 (1966); H. E. Stanley, *ibid.* **20**, 589 (1968).
[3] M. A. Moore, Phys. Rev. Lett. **23**, 861 (1969).
[4] W. J. Camp and J. V. Van Dyke, J. Phys. C **8**, 336 (1975).
[5] F. J. Wegner, Z. Phys. **206**, 465 (1967).
[6] V. L. Berezinskii, Zh. Eksp. Teor. Fiz. **59**, 907 (1970) [Sov. Phys.—JETP **32**, 493 (1971)].
[7] J. M. Kosterlitz and D. J. Thouless, J. Phys. C **5**, L124 (1972); **6**, 1181 (1973); J. M. Kosterlitz, *ibid.* **7**, 1046 (1974).
[8] J. Villain, J. Phys. C **10**, 1717 (1977); **10**, 4793 (1977).
[9] D. L. Stein and M. C. Cross, Phys. Rev. Lett. **42**, 504 (1979).
[10] P. Bak, Solid State Commun. **32**, xxx (1979).
[11] S. Alexander and P. Pincus, J. Phys. A **13**, 263 (1980).
[12] T. Nattermann, J. Phys. C **14**, 2441 (1981).
[13] S. Teitel and C. Jayaprakash, Phys. Rev. B **27**, 598 (1983).
[14] D. H. Lee, R. G. Caflisch, J. D. Joannopoulos, and F. Y. Wu, Phys. Rev. B **29**, 2680 (1984).
[15] D. H. Lee, J. D. Joannopoulos, J. W. Negele, and D. P. Landau, Phys. Rev. Lett. **52**, 433 (1984).
[16] S. Miyashita and H. Shiba, J. Phys. Soc. Jpn. **53**, 1145 (1984).
[17] G. H. Wannier, Phys. Rev. **79**, 357 (1950).
[18] W. Y. Shih and D. Stroud, Phys. Rev. B **30**, 6774 (1984).

[19] T. C. Halsey, Phys. Rev. B **31**, 5728 (1985).

[20] D. R. Nelson and J. M. Kosterlitz, Phys. Rev. Lett. **39**, 1201 (1977).

[21] If two spins happen to be parallel or antiparallel, the helicity is defined to be zero.

[22] A different definition of the helicity of a triangle is $(2/3\sqrt{3})(\mathbf{S}_1\times\mathbf{S}_2+\mathbf{S}_2\times\mathbf{S}_3+\mathbf{S}_3\times\mathbf{S}_1)\cdot\hat{\mathbf{z}}$, where 1, 2, and 3 are, sequentially, the three vertices of the triangle when it is transversed in a clockwise fashion.

[23] K. Kirkpatrick. C. Gelatt, Jr., and M. Vecchi, Science **220**, 671 (1983).

[24] See, for instance, *Phase Transitions and Critical Phenomena,* edited by C. Domb and M. S. Green, Vol. I (Academic, New York, 1971), Vol. I.

[25] E. Müller-Hartmann and J. Zittartz, Z. Phys. B **27**, 261 (1977).

[26] T. Ohta and D. Jasnow, Phys. Rev. B **20**, 139 (1979).

[27] J. Goldstone, Nuovo Cimento **19**, 154 (1961).

[28] See, for example, L. D. Landau and E. M. Lifshitz, *Statistical Physics,* 3rd ed. (Pergammon, New York, 1980), Pt. I.

[29] For a review, see F. Y. Wu, Rev. Mod. Phys. **54**, 235 (1982).

[30] J. Ashkin and E. Teller, Phys. Rev. **64**, 178 (1943).

[31] K. Binder and D. Landau, Phys. Rev. B **13**, 1140 (1976); for a general description, see K. Binder, in *Monte Carlo Methods in Statistical Physics,* edited by K. Binder (Springer, Berlin, 1979).

[32] M. E. Fisher, in *Proceedings of the International Summer School "Enrico Fermi" 1970, Course 51,* Varenna, Italy, edited by M. S. Green (Academic, New York, 1971).

[33] For examples of the application of finite-size—scaling theory, see A. E. Ferdinand and M. E. Fisher, Phys. Rev. **185**, 832 (1969); D. P. Landau, Phys. Rev. B **13**, 2997 (1976); **14**, 255 (1976); **16**, 4164 (1977).

[34] M. F. Sykes, D. S. Gaunt, P. D. Roberts, and J. A. Wyles, J. Phys. A **6**, 624 (1972).

[35] M. Yosefin and E. Domany, Phys. Rev. B **32**, 1778 (1985).